Research article

Impact of non-covalent interactions on FT-IR spectrum and properties of 4-methylbenzylammonium nitrate. A DFT and molecular docking study

Mouna Medimagh [a], Noureddine Issaoui [a,*], Sofian Gatfaoui [b], Silvia Antonia Brandán [c], Omar Al-Dossary [d,**], Houda Marouani [b], Marek J. Wojcik [f]

[a] University of Monastir, Laboratory of Quantum and Statistical Physics (LR18ES18), Faculty of Sciences, Monastir, 5079, Tunisia
[b] University of Carthage, Laboratory of Chemistry of Materials (LR13ES08), Faculty of Sciences of Bizerte, 7021, Tunisia
[c] Cátedra de Química General, Instituto de Química Inorgánica, Facultad de Bioquímica, Química y Farmacia, Universidad Nacional de Tucumán, Ayacucho 471, 4000, San Miguel de Tucumán, Tucumán, Argentina
[d] Department of Physics and Astronomy, College of Science, King Saud University, PO Box 2455, Riyadh, 11451, Saudi Arabia
[f] Faculty of Chemistry, Jagiellonian University, 30-387 Krakow, Gronostajowa 2, Poland

ABSTRACT

In this research, the impact of non-covalent interactions on the FT-IR spectrum and structural, electronic, topological and vibrational properties of hybrid 4-methylbenzylammonium nitrate (4MBN) have been studied combining B3LYP/CC-PVTZ calculations with molecular docking. 4MBN was synthesized and characterized by using the FT-IR spectrum while the optimized structures in gas phase and in ethanol and aqueous solutions have evidenced monodentate coordination between the nitrate and methylbenzylammonium groups, in agreement with that experimental determined for this species by X-ray diffraction. Here, non-covalent interactions were deeply analyzed in terms of topological parameters (AIM), electron localization function (ELF), localized orbital locator (LOL), Hirshfeld surface and reduced density gradient (RDG) method. Weak interactions such as H-bonds, VDW and steric effect in 4MBN were visualized and quantified by the independent gradient density (IGM) based on the promolecular density. The hyper-conjugative and the delocalization of charge in 4MBN have been elucidated by natural bonding orbital (NBO) while its chemical reactivity was studied and discussed by using molecular electrostatic potential surface (MESP), frontier molecular orbital (FMOs), density of state (DOS) and partial density of state (PDOS). The complete vibrational assignments of 69 vibration modes expected for 4MBN are reported together with the scaled force constants while the electronic transitions were evaluated by TD-DFT calculations in ethanol solution. Thermal analysis (DTA and DSC) was also determined. Molecular docking calculations have suggested that 4MBN presents biological activity and could act as a good inhibitor against schizophrenia disease.

1. Introduction

In recent years, molecular modelling has become a widely used tool for research and modelling new chemical compounds because it is a handy technical to reconstruct the structures of molecules from experimental data. Numerous experimental and theoretical studies have been carried out for a better prediction and understanding of the structures, molecular interactions and various properties of chemical species [1]. Thus, many studies on the most important inter and intra-molecular interactions have allowed describing, measure and comprehending their nature [1, 2]. In particular, the weak interactions are well known in

various physical, chemical and biological fields [2] while the non-covalent interactions exist in the crystal structure of hybrids to ensure maintain the geometry of large molecules. In fact, the concept of "hybrid material" is utilized in many applications because it combines both organic and inorganic entities. In this research work, we have studied the hybrid material, 4-4-methylbenzylammonium nitrate (4MBN) whose structure was already determined by X-ray diffraction [3]. This material consists of an organic unit which is 4-methylbenzylammonium and an inorganic unit which is nitric acid. This type of material which combines the nitrate anion with the organic molecule has attracted attention due to their many uses in different fields, such as
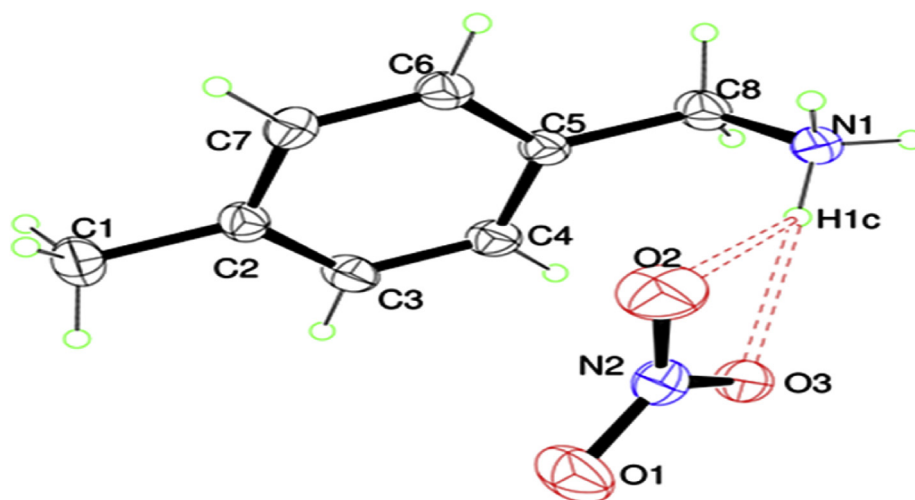
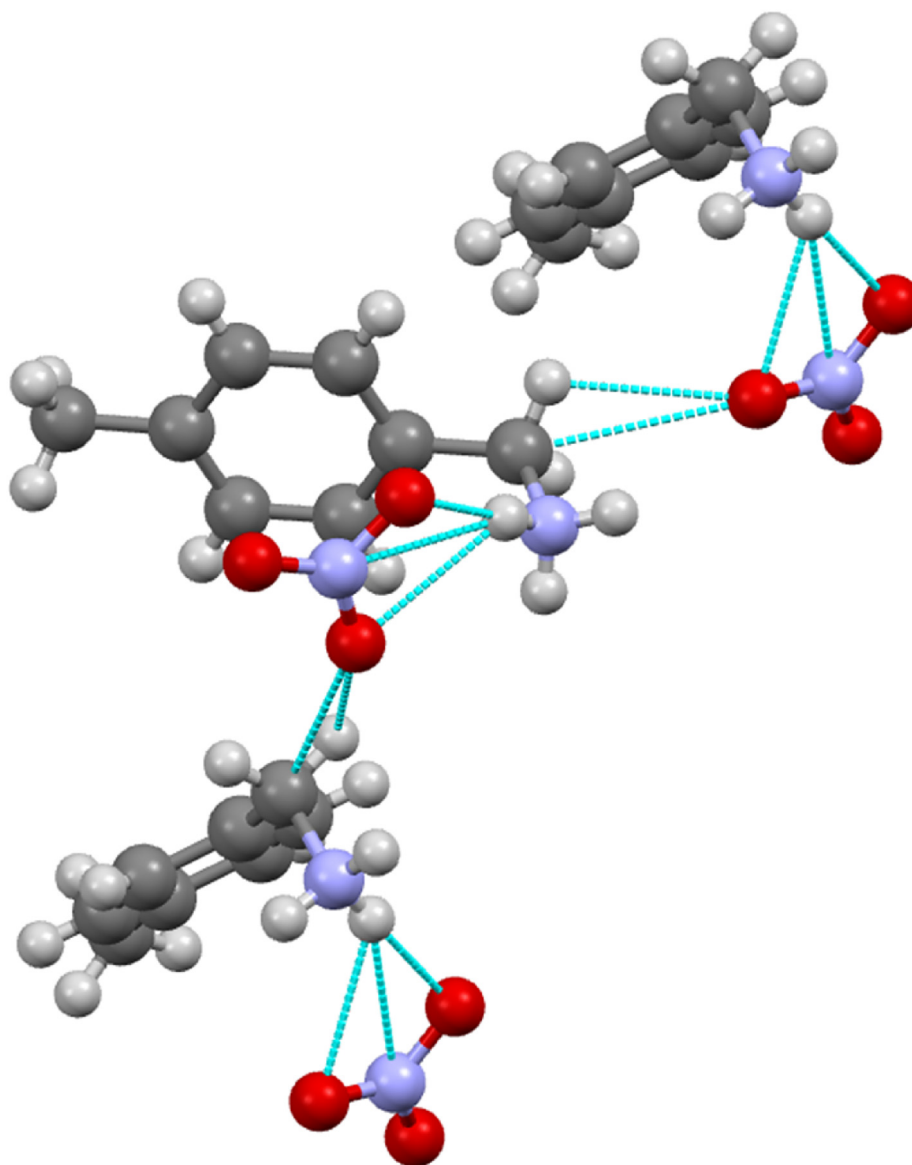**Figure 1.** ORTEP representation of 4-methylbenzylammonuim nitrate.

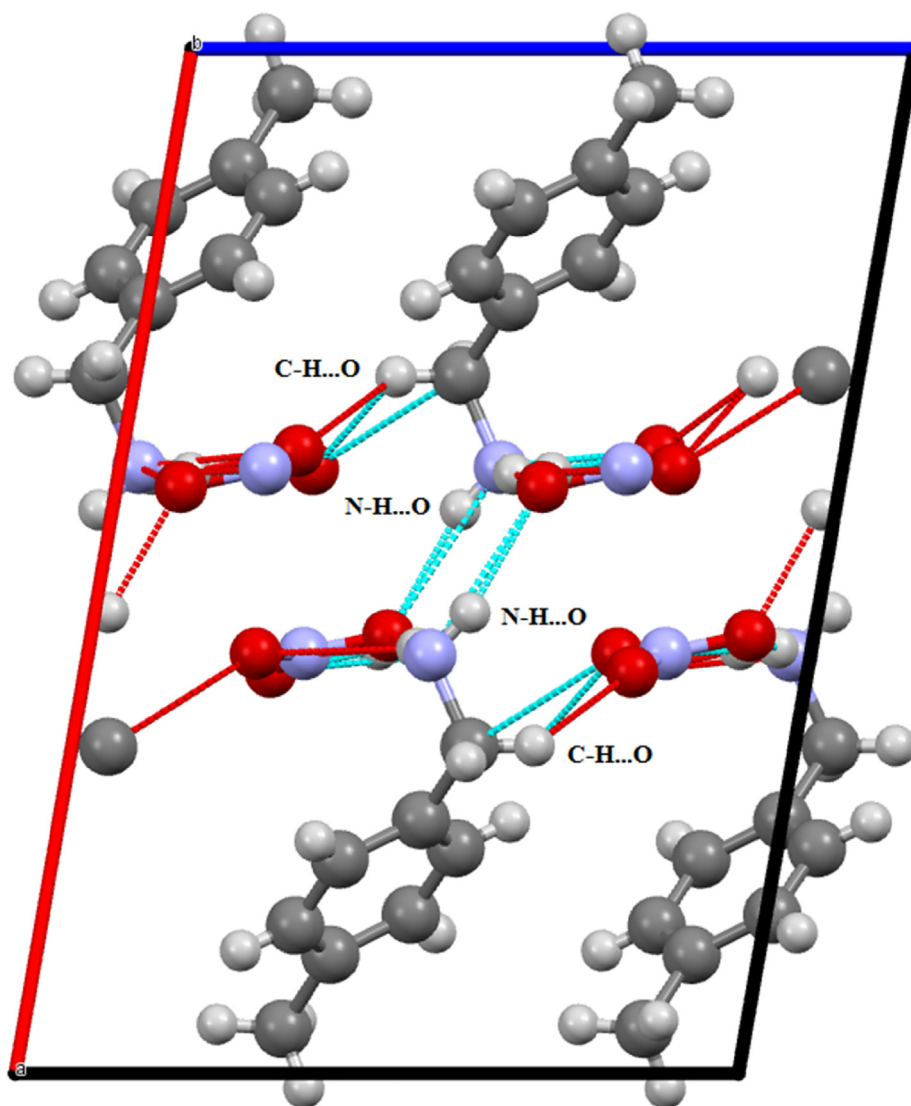**Figure 2.** Graphical representation of hydrogen bonds: N-H…O and C-H…O.

Figure 3. Graphical representation of hydrogen bonds.

biomolecular science, liquid crystals, catalysts and fuel cells [4]. So far, the vibrational study, complete vibrational assignments and properties of 4MBN even not were reported yet. Hence, one of aim of this work is the vibrational study of 4MBN by using the FT-IR spectrum, the normal internal coordinates and the SQMFF methodology in order to analyze the coordination mode between inorganic and organic species based on the corresponding vibration modes and taking into account assignments for similar species [5, 6, 7, 8]. To achieve this purpose, DFT calculations were employed to study the structure and physico-chemical properties in order to reproduce with great precision the experimental structure and the FT-IR spectrum of 4MBN. Other of the objectives is to study the non-covalent interactions from a theoretical point of view using atoms in molecule (AIM) approach, electron localization function (ELF) and localized orbital locator (LOL). Hirshfeld surface have been used in order to analyze intra and intermolecular interactions in the crystal structure 4MBN. Reduced density gradient (RDG) and independent gradient density (IGM) were performed also to reveal the weak interactions. Natural bonding orbitals (NBO) analysis was used to determine the different donor-acceptor interactions presents in 4MBN while the molecular electrostatic potential surface (MESP) was displayed to identify its electrophilic and nucleophilic sites. The reactive sites were evaluated by using the frontier molecular orbital (FMOs) while the character of the molecular orbitals (MO) and the contribution of each group in 4MBN

were illustrated by means of graphics of density of state (DOS) and partial density of state (PDOS). The UV-Visible absorption spectroscopy computes the major absorption features: excitation energy (E), Absorption wavelength (λ), oscillator force (f) and major contribution of the electronic transitions using TD-DFT method. Further, thermal analysis was reported here. In the pharmaceutical field, the 4MBN has promising use, as an intermediate pharmaceutical compound. It is popularly used to treat anxiety disorders as Schizophrenia diseases. Because of this, and because of the very important properties of this compound, we were encouraged to study the biological activities of our compound. Thus, by using the molecular docking method to assess the activity of quarter ligands (4MBN, BEZ, FAD and 98B) described in the literature as potential inhibitors of DAO protein. The objective of this method is to understand the mechanisms of action of this protein (DAO) and its role in the treatment of schizophrenia disease.

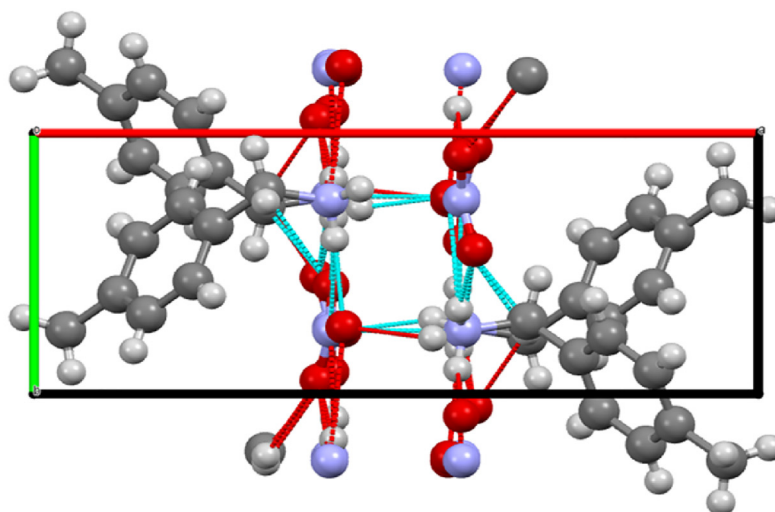## 2. Experimental and computational details

2.1. Physical measurements

Reagents were purchased from Sigma Aldrich Company.

The IR spectrum was obtained on a Perkin-Elmer Spectrum BX II FT-IR spectrometer using a sample dispersed in a spectroscopically pure KBr
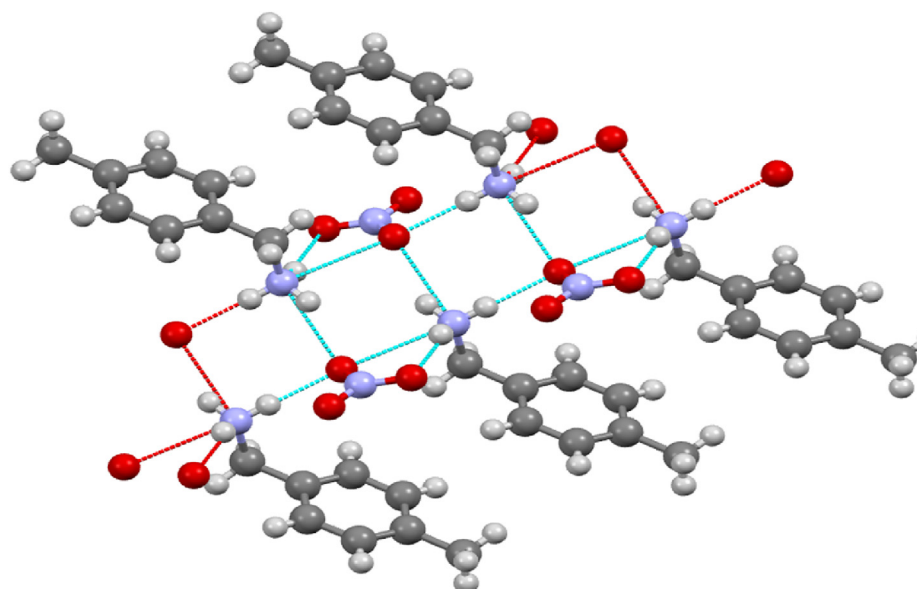
(a) along the axis b

(b) along the axis c

Figure 4. Crystal structure of 4MBN: (a) along the axis b and (b) along the axis c.

pellet in the 400–4000 cm^{-1} region. The spectral resolution was 4 cm^{-1}. UV-Vis spectrum was recorded on a Perkin Elmer Lambda 19 spectrophotometer using quartz cuvettes with 1cm optical path in the 200–800 nm range. This technique involves adding to the cuvette a solution of the sample in 2 mL of ethanol with a concentration of 2.10^{-3} mol.L^{-1}. The spectral resolution was 2 nm.

The thermal analysis of the synthesized compound is carried out using a multimodule 92 Setaram analyzer under argon. The mass of product was 10.2 mg for DTA-TG and 11.21 mg for DSC placed in a platinum crucible from room temperature up to 880 K for DTA-TG and in the range temperature [298–535 K] for DSC with a heating rate of 5 K.min^{-1}.

2.2. X-ray diffraction analysis

The experimental structure of 4MBN was determined by X-ray diffraction at room temperature (293 K) [3]. This analysis revealed that 4MBN belongs to the monoclinic crystal system with the space group P2$_1$/c and their lattice parameters are as follows: a = 15.097 (2) Å, b = 5.812 (10) Å, c = 10.486 (2) Å and β = 99.75 (2)° [3]. Figure 1 shows an

ORTEP plot of 4MBN with displacement ellipsoids drawn at the 30% probability level. The molecular structure consists of an organic cation which is 4-methylbenzylammonium and an inorganic anion NO$_3$. In the crystal structure, molecules develop in parallel layers along the b axis and along the c axis are described by a succession of cationic and anionic layers (Figure 2). In addition Figures 3 and 4 indicates that the crystal cohesion and stability between cationic and anionic entities is ensured by two types of weak hydrogen bonds: C-H…O and N-H… O. These two interactions were evaluated by different computational and experimental methods, as we will see later.

2.3. Computational details

In the present study, all calculations were performed by using Gaussian 09 [9] program and *GaussView* 6.0 [10] as interface visualization. The molecular geometry structure has been optimized with density functional theory (DFT) using the hybrid functional B3LYP (Becke's three parameter hybrid functional using the LYP correlation functional) [11, 12] with CC-PVTZ basis set. The non-covalent interactions were
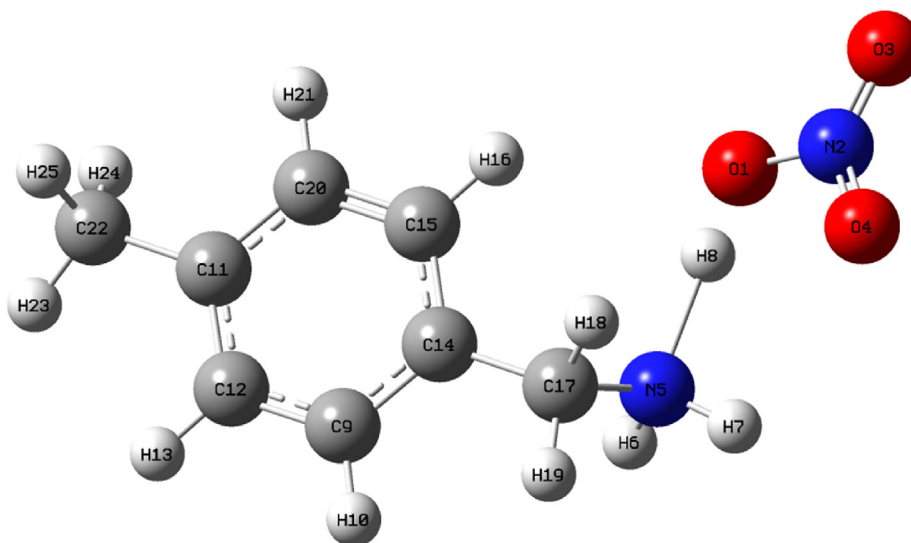
Figure 5. Optimized molecular structure of 4MBN.

Table 1. Energies and dipole moment values in gas and solvent phase with/without dispersion effect.

Méthode	DFT/B3LYP/CC-PVTZ			
	Gas without dispersion	Water without dispersion	Gas with dispersion	Water with dispersion
Energy (a.u)	-647.440	-647.413	-647.404	-647.435
Dipolar moment (D)	5.7	15	4.6	14.2

examined in detail with AIM, ELF, LOL, RDG and IGM analysis using Multiwfn program [13] and the isosurfaces are visualized via VMD software package [14]. Also, the Hirshfeld surface has been generated using Crystal Explorer 3.1 program [15]. A natural orbital bond (NBO) analysis was carried out to study the transfer of electronic charge (donor-acceptor) in the molecule and the bond orders. The molecular electrostatic potential surface (MESP) was mapped to identify the electrophilic and nucleophilic sites which promote the formation of hydrogen bonds in 4MBN. The complete vibrational assignments of all bands observed in the experimental FT-IR spectrum of 4MBN in gas phase were performed with the calculated harmonic force fields by using the scaled quantum mechanical force field (SQMFF) methodology and taking into account the normal internal coordinates, transferable scaling factors and the Molvib program [16, 17, 18]. The experimental structure has evidenced that NH_2 group is coordinate to H atom of OH of acid and, hence, it is as NH_3 group, for which this group was considered with C_{3V} symmetry while the NO_3 group with C_{2V} symmetry because it group was optimized with two double bonds character and the other one as simple bond, as was observed in similar species [5, 6, 7, 8]. Also, UV-Vis spectra and electronic properties such as frontier molecular orbital analysis (HOMO–LUMO) were computed with the help of time-dependent DFT (TD-DFT) method. Plots of state density (DOS) and partial state electron density (PDOS) were obtained using GaussSum software [19]. Finally, the molecular docking has been performed for the determination of biological activity and to analyze various ligand-receptor interactions. In addition, the structures ligands and protein are extracted from the PDB data bank (Protein Data Bank) [20]. The docking calculations were carried out by using iGEMDOCK program [21] and the results obtained were visualized using discovery studio software [22].

3. Results and discussion

3.1. Optimized geometry of the molecule studied

The optimized structure of 4MBN obtained with the B3LYP/CC-PVTZ method is depicted in Figure 5. Table 1 presents the effect of dispersion on the values of minimum energies and dipolar moment (μ) in the gas phase and in the presence of a solvent (water). The examination of this table shows that the optimization in the gas without dispersion is the most stable because it has the minimum energy value (E = -647.440 a.u). The dipole moment is high in water (μ (dispersion) = 15 D and μ (without dispersion) = 14.2 D) compared to gas (μ (dispersion) = 4.6 D and μ (without dispersion) = 5.7 D), which indicate the increase of the polar character and charge separation in water.

To see how well the theoretical model represents reality, an RMSD (Root Mean Square Deviation) calculation was performed to compare between the experimental and theoretical values. RMSD values (Table 2) shows that the dispersion has a weak effect on the calculated bond lengths in the gas phase unlike the solvent (water). For bond angles, the dispersion shows a small change in gas phase and solvent. The lowest RMSD values are noted for bond lengths (0.012 Å) and 0.965° for angles in water with and without dispersion, respectively. The graphs of correlations between theoretical and experimental distances and bond angles in gas phase and in solvent with and without dispersion are shown in Figures 6, 7, 8, and 9. The values of R^2 (Table 2) are very close to 1, so we can say that all the parameters calculated are agreeing well with the experiment. The geometric parameters such as the bond length and bond angle are compared with the experimental results as presented in Table 2. The bond angle of intramolecular hydrogen bonding interaction (N-H ⋯... O) has found to be 106.550°. 4MBN has eight C-C bond lengths, three O-N bond lengths, a single C-N bond and hydrogen bonds. Theoretically, the C-C intermolecular bond lengths of the benzene group are: C_9-C_{14} (1.392 Å), C_9-C_{12} (1.391 Å), C_{11}-C_{20} (1.398 Å), C_{11}-C_{12} (1.392 Å), C_{15}-C_{20} (1.386 Å) and C_{14}- C_{15} (1.397 Å). It is noticed that the values of the computed geometric parameters are slightly different compared to the experimental ones. This difference is explained by the fact that the experimental results are obtained from a solid state where the packing forces were not considered because the calculations were performed in the gaseous state for the molecules isolated. These differences also are observed in the broad band observed in the FT-IR spectrum in the 4000-2000 cm^{-1} region.

Table 2. Comparison between experimental and calculated geometric parameters of 4MBN compound.

	Geometric parameters				Exp
	Gas		water		
	without dispersion	with dispersion	without dispersion	with dispersion	
Bond lengths (Å)					
O_1-N_2	1.368	1.218	1.268	1.268	1.240 (2)
O_1-H_8	1.038	1.015	1.763	1.748	2.010
N_2-O_3	1.201	1.014	1.245	1.244	1.253 (2)
N_2-O_4	1.220	1.641	1.249	1.248	1.219 (2)
N_5-H_6	1.014	1.487	1.020	1.020	0.890
N_5-H_7	1.015	1.084	1.020	1.019	0.890
N_5-H_8	1.620	1.389	1.045	1.044	0.890
N_5-C_{17}	1.484	1.392	1.507	1.508	1.464 (3)
C_9-H_{10}	1.083	1.393	1.083	1.083	0.930
C_9-C_{12}	1.391	1.396	1.388	1.388	1.379 (3)
C_9-C_{14}	1.391	1.505	1.395	1.394	1.382 (3)
C_{11}-C_{12}	1.392	1.083	1.397	1.397	1.378 (3)
C11-20	1.397	1.394	1.396	1.395	1.382 (3)
C_{11}-C_{22}	1.505	1.506	1.504	1.503	1.508 (3)
C_{12}-H_{13}	1.082	1.082	1.083	1.082	0.930
C_{14}-C_{15}	1.397	1.386	1.394	1.393	1.384 (2)
C_{14}-C_{17}	1.507	1.090	1.502	1.500	1.505 (3)
C_{15}-H_{16}	1.082	1.094	1.083	1.082	0.930
C_{15}-C_{20}	1.385	1.083	1.389	1.389	1.377 (3)
C_{17}-H_{18}	1.091	1.090	1.086	1.086	0.970
C_{17}-H_{19}	1.092	1.093	1.086	1.086	0.970
C_{20}-H_{21}	1.083	1.090	1.083	1.082	0.930
C_{22}-H_{23}	1.089	1.218	1.090	1.090	0.961
C_{22}-H_{24}	1.090	1.015	1.090	1.09	0.960
C_{22}-H_{25}	1.092	1.014	1.093	1.093	0.960
RMSD	**0.138**	**0.105**	**0.083**	**0.012**	-
R^2	**0.969**	**0.983**	**0.954**	**0.986**	
Bond angles (°)					
N_2-O_1-H_8	106.550	105.969	109.642	107.912	104.130
O_1-N_2-O_3	115.377	115.161	119.421	119.362	118.8 (2)
O_1-N_2-O_4	117.069	117.175	119.575	119.520	121.1 (2)
O_3-N_2-O_4	127.552	127.663	121.002	121.113	120.2 (2)
H_6-N_5-H_7	107.742	107.720	108.027	108.418	109.5
H_6-N_5-H_8	115.430	98.741	108.073	107.611	109.5
H_6-N_5-C_{17}	110.136	109.846	110.588	110.315	109.4
H_7-N_5-H_8	99.660	116.260	108.777	109.487	109.5
H_7-N_5-C_{17}	109.922	110.850	110.612	110.977	109.4
H_8-N_5-C_{17}	113.253	112.540	110.674	109.953	109.5
H_{10}-C_9-C_{12}	119.443	119.532	119.712	119.934	119.6
H_{10}-C_9-C_{14}	119.598	119.680	119.635	119.533	119.6
C_{12}-C_9-C_{14}	120.958	120.785	120.652	120.528	120.7 (2)
C_{12}-C_{11}-C_{20}	117.866	118.023	118.025	118.164	117.5 (2)
C_{12}-C_{11}-C_{22}	121.349	121.228	120.938	120.799	121.3 (2)
C_{20}-C_{11}-C_{22}	120.777	120.730	121.027	121.024	121.23 (2)
C_9-C_{12}-C_{11}	121.010	120.981	121.031	120.976	121.5 (2)
C_9-C_{12}-C_{13}	119.449	119.5	119.507	119.618	119.3
C_{11}-C_{12}-H_{13}	119.539	119.516	119.461	119.404	119.2
C_9-C_{14}-C_{15}	118.206	118.417	118.605	118.812	118.1 (2)
C_9-C_{14}-C_{17}	120.667	120.677	120.494	120.325	121.5 (2)
C_{15}-C_{14}-C_{17}	121.123	120.769	120.896	120.756	120.4 (2)
C_{14}-C_{15}-H_{16}	119.823	119.708	119.648	119.568	119.7
C_{14}-C_{15}-C_{20}	120.705	120.716	120.578	120.517	120.6 (2)
H_{16}-C_{15}-C_{20}	119.469	119.553	119.771	119.892	119.7
N_5-C_{17}-C_{14}	111.539	109.921	111.306	110.243	112.2 (2)

Table 2 (*continued*)

	Geometric parameters				Exp
	Gas		water		
	without dispersion	with dispersion	without dispersion	with dispersion	
N_5-C_{17}-H_{18}	106.698	107.251	106.345	106.525	109.2
N_5-C_{17}-H_{19}	111.300	111.431	106.837	106.908	109.2
C_{14}-C_{17}-H_{18}	110.635	110.473	111.639	111.781	109.2
C_{14}-C_{17}-H_{19}	109.298	110.107	111.529	112.003	109.2
H_{18}-C_{17}-H_{19}	107.262	107.594	108.929	109.116	107.9
C_{11}-C_{20}-C_{15}	121.251	121.058	121.106	120.998	121.5 (2)
C_{11}-C_{20}-H_{21}	119.448	119.486	119.461	119.478	119.2
C_{15}-C_{20}-H_{21}	119.300	119.452	119.432	119.520	119.2
C_{11}-C_{22}-H_{23}	111.441	111.601	111.362	111.320	109.5
C_{11}-C_{22}-H_{24}	111.341	110.455	111.311	111.429	109.5
C_{11}-C_{22}-H_{25}	111.028	111.451	110.867	110.668	109.5
H_{23}-C_{22}-H_{24}	108.101	107.616	108.543	108.556	109.5
H_{23}-C_{22}-H_{25}	107.607	108.231	107.179	107.265	109.5
H_{24}-C_{22}-H_{25}	107.127	107.302	107.394	107.423	109.4
RMSD	**1.535**	**1.635**	**0.965**	**1.077**	-
R^2	0.993	**0.995**	**0.959**	**0.995**	

3.2. Non-covalent interaction analysis

3.2.1. Topological analysis

3.2.1.1. Quantum theory of atoms in molecules AIM. Quantum theory of atoms in molecules (QTAIM) theory is broadly used to study non-covalent interactions and it is initially developed by Bader [23, 24]. This approach has extensively been applied to identify the nature of bond critical points (BCPs) and to evaluate their energies. Generally, topological analysis has been used to classify hydrogen bond (weak, moderate, strong) and analyze the nature of interactions in terms of electron density ρ (r) and his Laplacien $\nabla^2\rho$ (r) inside the molecular systems [25]. The - G (r)/V (r) ratio in AIM analysis which describes the nature of the hydrogen bond [26]. In fact, when - (G (r)/V (r)) > 1, the hydrogen bond has a character non-covalent, whereas for 0.5 <- (G (r)/V (r)) <1, the hydrogen bond is covalent. Further, the topological properties are handy tool to characterize the strength of hydrogen bond such as: electron density ρ (r), and its Laplacian $\nabla^2\rho$ (r), kinetic energy density G (r), potential V (r), total energy H (r) and the bond energy E_{HB} = V (r)/2 (proposed by Espinosa and his collaborators [27]) are also the efficient parameters to characterize the hydrogen bonding. The various bond critical points (BCPs), new ring critical points (NRCPs) and ring critical points (RCPs) were identified as shown in Figure 10. Their corresponded topological parameters are provided in Tables 3 and 4. Inspection of the table shows that the low values of the ellipticity at the RCP points confirm that there is delocalization of electrons in the aromatic nucleus. In addition, the high value of ellipticity suggests that there is a strong delocalization in NRCP structures. As shown in Figure 3, the interactions between the monomer, dimer, around organic cation and around inorganic anion are mainly ensured by two types of hydrogen bonds: N-H···O and C-H···O. Basing on the values of $\nabla^2\rho$(r) et G(r) +V(r) are all positive in various cases as well as the $E_{interaction}$ is less than 12.0 kcal/mol (50 kJ/mol). These results confirm that the hydrogen bonds forming within our compound are considered weak. The ratio 0.5 <- (G (r)/V (r)) <1, indicating also that low hydrogen bonds existing in our compound are non-covalent nature. Moreover, the interactions of hydrogen bonds can be characterized by various important aspects, including the energy of ΔE bonds in the case of charged and neutral complexes [28]. In this context, the values of $\Delta E < 2.5$ kcal/mol, therefore the hydrogen bonds of our compound are weak and dominated by dispersions and electrostatic interactions.
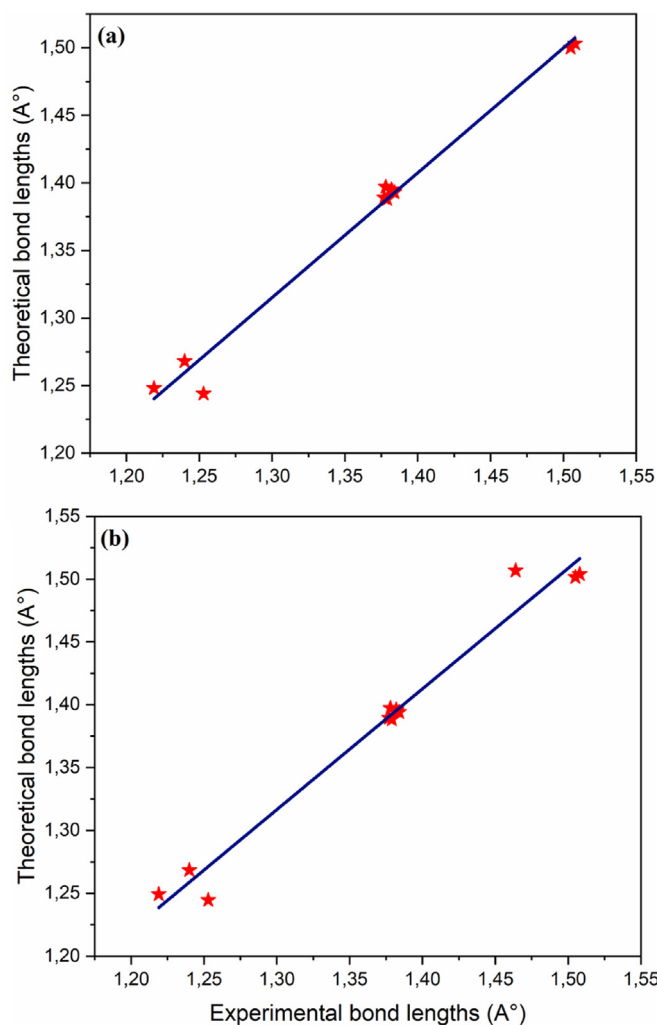
Figure 6. Correlations between theoretical and experimental lengths in the gas phases: (a) with and (b) without dispersion.

Figure 7. Correlations between theoretical and experimental lengths: (a) with and (b) without dispersion: solvent effect.

3.2.1.2. Electron localization function analysis (ELF). The topological analysis of the ELF [29, 30] is a powerful tool for determining the localization of electron pairs probability. It also helps to understand the behavior of electrons in multielectronic systems. This approach was generated by Silvi and Savin [30], it allows to decide if the electrons are localized. In fact, when the electrons are perfect localized the value of ELF varies in the range [0.5, 1], whereas an ELF $\leq 1/2$ shows the delocalized electronic region [31]. Furthermore, ELF furnishes some local measure of Pauli repulsion which is associated directly with the kinetic energy of electrons. Usually, the ELF value is close to 1 for the regions with the highest Pauling repulsion and is close to 0 for the regions with the lowest Pauling repulsion. The Figure 11 illustrates the ELF map of the title compound 4MBN on the plane C_{22}, N_5, N_2 atoms. A color code is represented with the ELF map varies from blue to red which show the scale range from 0 to 1. We can see from the 2D carte that the areas presented by a blue color around some carbon such as C_{22}, C_{14}, C_{11} and oxygen atoms (O_3) represent the delocalized electron. Whereas, the red and orange color around the hydrogen atoms of the organic group $C_8H_{12}N^+$ have comparatively large ELF values. Therefore, this region can be associated with a covalent bond character which is characterized by an appreciable electron density (a region of maximum Pauli repulsion). Generally, the elevated ELF regions are indicated a high localization of electrons, and may be identified with presence of a covalent bond, a lone pair of electrons, or a nuclear shell in that region. The visualization of the
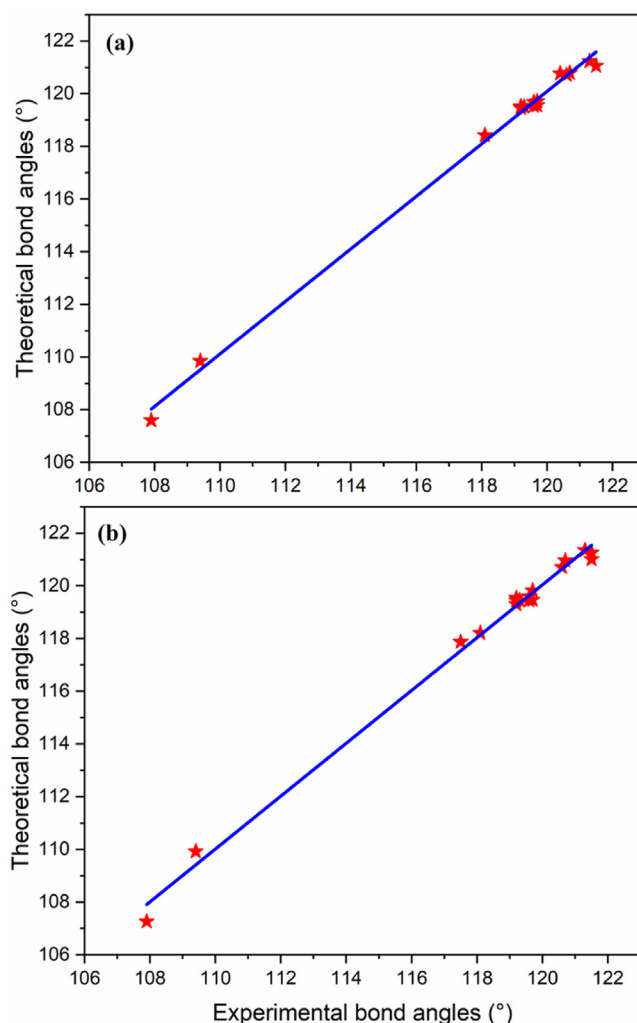
ELF can also indicate the non-covalent interactions (hydrogen bonds). Here, we noted that the ELF value is high around N_5-H_8 bond of the organic group (red region) and low around the O_1 atom of the inorganic group (blue circle). In addition, the blue region between the hydrogen atom H_8 and oxygen O_1 gave evidence for occurrence of interaction in this region, leading to a hydrogen bond of N-H ··· O type. Not only, the other types of hydrogen bonds can be displayed in the crystal structure of our compound. Therefore, we can conclude that this method is in agreement with the AIM approach.

3.2.1.3. Localized orbital locator (LOL) theory. Electron localization descriptor such as localized orbital locator (LOL) is widely used to describe the molecular bonding, reactivity and chemical structure. This tool is similar to the ELF as both depend on the kinetic energy density [32]. LOL analysis was introduced by Silvi and Savin [30] and carried out by using Multiwfn software. Also, the LOL map is a simpler and clearer picture than ELF. Moreover, ELF explains the electron pair density and LOL illustrates highestlocalized orbitals overlapping owing to the gradients of orbitals. Color filled map of the LOL for the atoms of the title compound is summarized in the Figure 12. According to this figure, we observed that the high limit for LOL is 0.8 (red) and the lower limit is 0 (blue). LOL achieves in high regions (superior in 0.5) when the electron density is dominated by electron localization. It is seen in the Figure 11 that the region represented by the blue color around the carbon and nitrogen atoms provides LOL values ≤ 0.5 (region where the electron
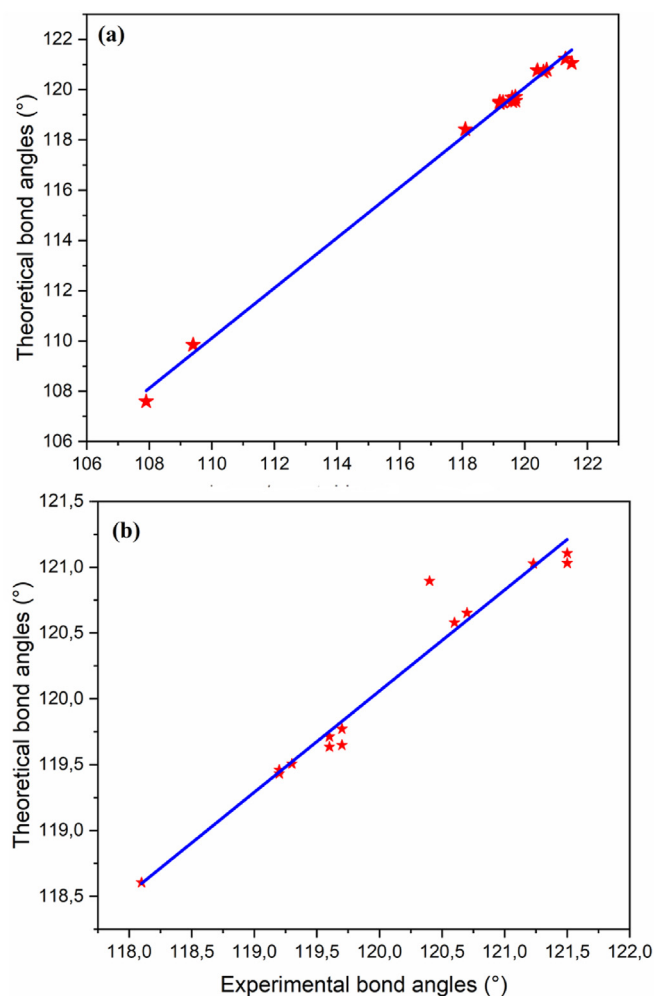
Figure 8. Correlations between theoretical and experimental angles in the gas phases: (a) with and(b) without dispersion.

density is considerably depleted). Therefore the bonds could be classified in this region as weakly covalent bond or van der Waals bonds. Furthermore, the red color region near carbon atoms of the benzene ring with strong LOL values are due covalent bonds between the atoms (region where the electron density is much concentrated). As a result of the presence of a covalent bond in that area results in high localization of electrons, which proves great value in that region [32]. Also the small white circles present at the central part of the hydrogen atoms with maximum range caused to electron density (a region exceeds the high limit 0.8). As it is shown also in the figure of LOL that the low blue region between hydrogen H_8 and nitrogen N_5 displays the formation of a weak hydrogen bond of the N-H$\cdots$ O type. Similar to ELF, LOL confirms also the results found in AIM analysis.

3.2.2. Hirshfeld surfaces analyses (HS)

3D Hirshfeld surfaces (HS) and 2D fingerprint maps are unique for every molecule in the asymmetric unit of crystal structures. Indeed, (HS) provide a three-dimensional image of intermolecular interactions in crystals, while two-dimensional plots obtained by analysis of (HS) can identify each type of intermolecular interaction. The d_{norm} molecular (HS), "d_e", Shape index and "Curvedness" of $(C_8H_{12}N)\ NO_3$ are respectively shown in Figure 13. These surfaces are shown transparent to highlight the visualization of the orientation and conformation of functional groups in the crystal. The normalized contact distance (d_{norm}) of the produced compound displays a surface with a color scheme (red, blue, white), where the red spots highlight the shortest intermolecular
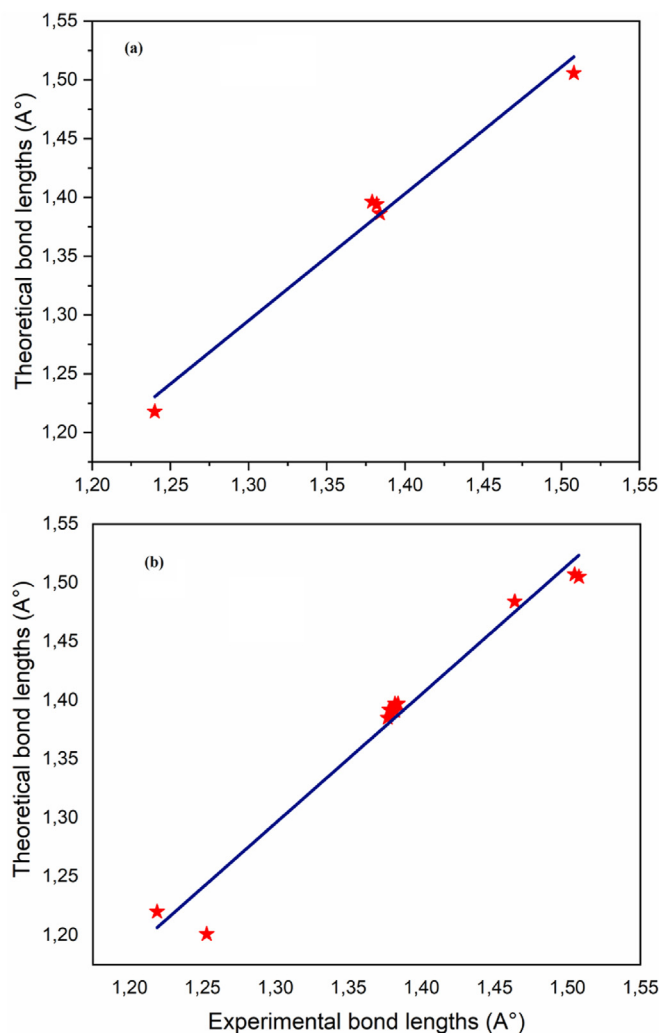

Figure 9. Correlations between theoretical and experimental angles (a) with and (b) without dispersion: solvent effect.

contacts which are attributed to the N-H$\cdots$ O and C-H interactions. $\ldots$ O. The blue areas indicate the most linguistic intermolecular contacts in the structure and the white areas represent the contacts around the van der Waals separation. The latter correspond respectively to the interactions H$\ldots$ H, N$\ldots$H and C$\ldots$ H [33, 34, 35, 36]. These contacts have been observed on the d_e map where the large orange spots attributed to the N-H $\ldots$ O hydrogen bonds, while the small blue spots correspond to the H $\ldots$ H, C $\ldots$ H and N $\ldots$ H contact. The absence of red and blue triangles on the Shape index map and the small flat segments delimited by blue outlines on the curvedness map exclude the presence of π-π and C-H$\ldots$ π interactions in our crystal structure [36].

Electrostatic potential plays a key role in molecular recognition processes, including interactions with drug receptors. Again it exhibits important properties for the evaluation of lattice energy in crystals [37, 38]. The electrostatic potentials of $(C_8H_{12}N)\ NO_3$ were mapped on the (HS) using the STO-3G base fixed at the level of Hartree-Fock theory over a range of ± 0.20 AU. Indeed, the presence of interactions and hydrogen bonds C-H$\ldots$ O and N-H$\ldots$ O between anions and cationic groups are observed through their (HS) mapped to the electrostatic potential (Figure 13 c). This map shows donor atoms (Nitrogen and Carbon of $C_8H_{12}N^+$) in blue regions with positive potential and acceptor atoms (Oxygen of NO_3^-) with negative potential in red regions [39, 40, 41].

The overall two-dimensional fingerprint plot as well as the percentages of the various contacts existing in the $(C_8H_{12}N)\ NO_3$ compound is
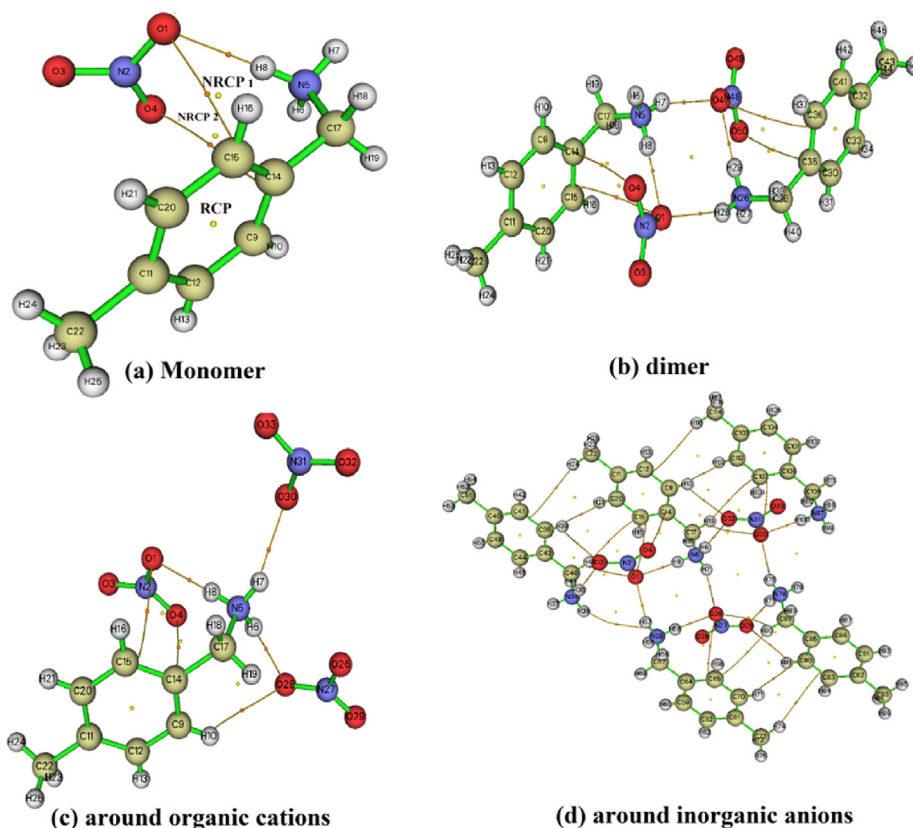
Figure 10. Graphic representation of critical points in: (a) monomer, (b) dimer, (c) around organic cations and (d) around inorganic anions.

Table 3. Topological parameters of critical points in monomer and dimer from.

Interaction	$\nabla^2\rho(r)$ (u. a)	$\rho(r)$ (u. a)	$G(r)$ (u. a)	$V(r)$ (u. a)	$H(r)$ (u. a)	ε	$E_{interaction}$ (kJ/mol)
Monomer							
RCP	0.025	0.159	0.036	-0.033	0.004	-1.233	-
NRCP1	0.005	0.016	0.003	-0.002	0.001	-3.957	-
NRCP2	0.003	-0.002	0.002	-0.002	0.001	2.777	-
$O_1...H_8-N_5$	0.025	0.074	0.018	-0.018	0.002	0.045	-23.498
Dimer							
RCP1	0.025	0.159	0.036	-0.033	0.004	-1.231	-
RCP2	0.025	0.159	0.036	-0.033	0.004	-1.231	-
NRCP1	0.005	0.016	0.003	-0.002	0.001	-3.075	-
NRCP2	0.002	0.0072	0.001	-0.001	0.001	-1.397	-
NRCP3	0.005	0.016	0.003	-0.002	0.001	-3.075	-
NRCP4	0.003	0.011	0.002	-0.002	0.001	-2.487	-
NRCP5	0.003	0.011	0.002	-0.002	0.001	-2.487	-
$O_1...H_8-N_5$	0.024	0.078	0.019	-0.018	0.001	0.046	-23.63
$O_{47}...H_7-N_5$	0.017	0.067	0.014	-0.012	0.003	0.106	-15.36
$O_1...H_{28}-N_{26}$	0.017	0.067	-0.022	0.014	-0.012	0.003	-4.46
$O_1...C_{15}-H_{16}$	0.005	0.015	0.003	-0.002	0.001	2.352	-5.51
$O_4...C_{14}-C_9$	0.033	-0.011	0.111	-0.498	-0.387	0.201	-653.75
$O_{47}...C_{36}-H_{37}$	0.005	0.015	0.003	-0.002	0.001	2.352	-2.76
$O_{50}...C_{35}-C_3$	0.003	0.010	0.002	-0.002	0.001	2.270	-1.84

shown in Figure 13. d. In addition, Figure 14 represents the different contact which contributes in our molecule. H… H intercontacts (45.5%) have the greatest contribution on the (HS) with a maximum sum $d_e + d_i$ ~ 2.3 Å. H …... O/O ... H contacts comprise 37% of the entire (HS) and represented by two narrow, symmetrical pointed tips with $d_e + d_i$ ~ 1.9 Å. The C… H/H… C contacts show on its 2D graph the presence of two

wings centred around a sum $d_e + d_i$ ~ 2.79 Å. comparing the sum of the components of the pairs (d_i, d_e) of these contacts with the sum of the van der Waals radii of the atoms involved, we find that only the contacts O… H/H… O and C… H/H… C are considered to be close contacts with a sum $d_e + d_i$ less than or equal to the sum of the van der Waals radii of the atoms involved (H: 1.09 Å, O: 1.52 Å, C: 1.70 Å).

Table 4. Topological parameters of critical points around organic cation and around inorganic anion.

Interactions	$\nabla^2\rho(r)$ (a.u)	$\rho(r)$ (a.u)	$G(r)$ (a.u)	$V(r)$ (a.u)	$H(r)$ (a.u)	ε	$E_{interactions}$ (kJ/mol)
Around organic cation							
RCP	0.026	0.160	0.036	-0.033	0.004	-1.229	-
NRCP	0.003	0.010	0.002	-0.001	0.001	-2.718	-
NRCP	0.004	0.016	0.003	-0.002	0.001	-2.464	-
NRCP	0.003	0.014	0.003	-0.003	-0.002	-1.219	-
$O_1 \ldots H_8\text{-}N_5$	0.023	0.080	0.019	-0.017	0.001	0.024	-22.56
$O_{30} \ldots H_{17}\text{-}N_5$	0.016	0.068	0.0140	-0.011	0.003	0.077	-14.57
$O_{28} \ldots H_{10}\text{-}C_9$	0.005	0.017	0.346	-0.003	0.001	0.161	-3.28
$O_{28} \ldots H_6\text{-}N_5$	0.020	0.073	0.016	-0.014	0.002	0.017	-18.50
$O_1 \ldots C_{15}\text{-}H_{16}$	0.005	0.015	0.003	-0.002	0.001	1.491	-2.63
$C_{14} \ldots O_4\text{-}N_2$	0.031	0.010	0.002	-0.013	0.001	2.449	-17.07
Around inorganic anion							
RCP	0.026	0.159	0.036	-0.033	0.004	-1.232	-
RCP	0.026	0.159	0.036	-0.033	0.004	-1.232	-
RCP	0.025	0.159	0.036	-0.033	0.004	-1.232	-
RCP	0.026	0.159	0.036	-0.033	0.004	-1.231	-
RCP	0.026	0.159	0.036	-0.033	0.004	-1.231	-
NRCP	0.005	0.016	0.003	-0.002	0.001	-3.855	-
NRCP	0.002	0.010	0.002	-0.005	-0.001	-1.404	-
NRCP	0.002	0.009	0.002	-0.001	0.001	-1.351	-
NRCP	0.002	0.0010	0.002	-0.001	0.001	-1.419	-
NRCP	0.002	0.009	0.002	-0.001	0.001	-1.339	-
NRCP	0.002	0.008	0.001	-0.001	0.002	-1.335	-
NRCP	0.005	0.016	0.003	-0.002	0.001	-2.536	-
NRCP	0.002	0.007	0.001	-0.001	0.002	-1.393	-
NRCP	0.005	0.016	0.003	-0.002	0.001	-3.660	-
NRCP	0.004	0.005	0.001	-0.002	-0.002	-2.183	-
NRCP	0.003	0.014	0.003	-0.0017	0.001	-1.237	-
NRCP	0.003	0.015	0.003	-0.0018	0.001	-1.241	-
NRCP	0.006	0.023	0.005	-0.0034	0.001	-2.730	-
NRCP	0.002	0.010	0.002	-0.0010	0.001	-1.401	-
NRCP	0.002	0.010	0.002	-0.0010	0.001	-1.385	-
NRCP	0.002	0.006	0.001	-0.0008	0.001	-1.538	-
NRCP	0.003	0.014	0.003	-0.0018	0.001	-1.259	-
$C_{41} \ldots H_{24}\text{-}C_{22}$	0.003	0.010	0.002	-0.0011	0.001	2.317	-2.89
$O_3 \ldots H_{39}\text{-}C_{38}$	0.005	0.018	0.004	-0.0027	0.847	0.198	-7.09
$C_{15} \ldots H_{48}\text{-}C_{46}$	0.003	0.011	0.002	-0.0012	0.001	2.892	-1.58
$O_3 \ldots H_{35}\text{-}N_{34}$	0.021	0.072	0.016	-0.0147	0.002	0.042	-38.59
$O_1 \ldots H_{48}\text{-}C_{46}$	0.006	0.020	0.004	-0.0032	0.001	1.406	-4.20
$O_1 \ldots C_{15}\text{-}H_{16}$	0.005	0.015	0.030	-0.0022	0.001	1.771	-2.89
$O_1 \ldots H_8\text{-}N_5$	0.024	0.081	0.019	-0.0179	0.001	0.048	-23.50
$O_1 \ldots H_{57}\text{-}N_{55}$	0.017	0.068	0.014	-0.0117	0.003	0.133	-15.36
$O_4 \ldots C_{14}\text{-}C_9$	0.003	0.010	0.002	-0.0013	0.001	2.513	-1.71
$O_{26} \ldots H_7\text{-}N_5$	0.017	0.069	0.014	-0.0118	0.003	0.112	-15.49
$O_{26} \ldots H_{58}\text{-}N_{55}$	0.024	0.081	0.019	-0.0179	0.001	0.048	-23.50
$O_{26} \ldots C_{65}\text{-}H_{66}$	0.005	0.002	0.003	-0.0022	0.001	2.898	-2.89
$O_{26} \ldots H_{90}\text{-}C_{88}$	0.006	0.021	0.004	-0.0033	0.001	5.286	-4.33
$O_{28} \ldots H_{77}\text{-}N_{76}$	0.021	0.073	0.017	-0.0148	0.002	0.039	-38.86
$O_{28} \ldots H_{81}\text{-}C_{80}$	0.005	0.018	0.004	-0.0026	0.001	0.193	-3.41
$C_{65} \ldots H_{90}\text{-}C_{88}$	0.003	0.011	0.002	-0.0012	0.001	2.355	-1.56
$H_{71} \ldots H_{81}\text{-}C_{80}$	0.004	0.014	0.003	-0.0017	0.001	1.378	-2.23
$H_{57} \ldots H_{36}\text{-}N_{34}$	0.004	0.002	0.001	-0.001	-0.001	1.231	-1.58
$C_{83} \ldots H_{74}\text{-}C_{72}$	0.003	0.010	0.002	-0.001	0.001	3.170	-2.89
$C_{12} \ldots H_{116}\text{-}C_{114}$	0.003	0.010	0.002	-0.001	0.001	2.269	-2.89
$H_{10} \ldots H_{113}\text{-}C_{112}$	0.004	0.014	0.003	-0.002	0.001	1.387	-4.20
$C_{107} \ldots H_{19}\text{-}C_{17}$	0.003	0.011	0.002	-0.001	0.001	2.655	-1.58
$O_{32} \ldots H_{10}\text{-}C_9$	0.374	-0.017	0.125	-0.680	-0.555	0.023	-892.80
$O_{32} \ldots H_6\text{-}N_5$	0.021	0.073	0.016	-0.015	0.002	0.038	-38.59

Table 4 (*continued*)

Interactions	$\nabla^2\rho(r)$ (a.u)	$\rho(r)$ (a.u)	$G(r)$ (a.u)	$V(r)$ (a.u)	$H(r)$ (a.u)	ε	$E_{interactions}$ (kJ/mol)
$O_{30}...H_{100}-N_{97}$	0.024	0.080	0.019	-0.018	0.001	0.047	-23.24
$O_{30}...H_{78}-N_{76}$	0.017	0.068	0.014	-0.012	0.003	0.115	-15.49
$O_{30}...H_{19}-C_{17}$	0.056	0.021	0.004	-0.003	0.001	2.724	-4.20
$O_{30}...C_{107}-H_{108}$	0.005	0.015	0.003	-0.002	0.001	3.097	-2.89

⬥ RCP: Ring critical point.

⬥ NRCP: New ring critical point.

⬥ BCP: Bond critical point.
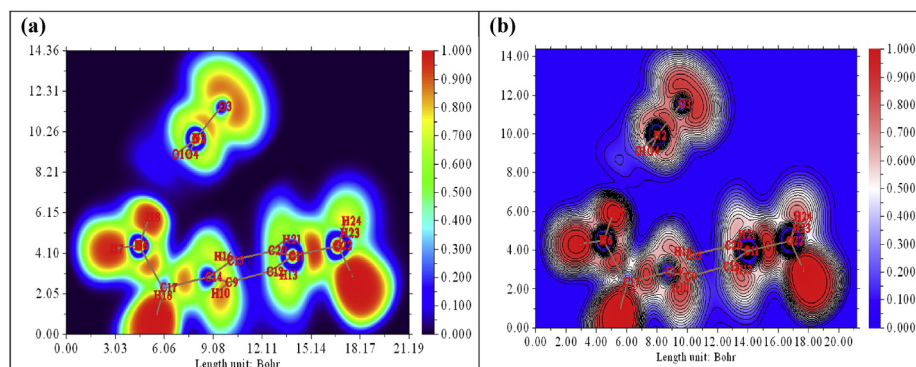
Figure 11. Graphs of electron localization function (ELF) maps of 4MBN on the plane C22, N5, N2 atoms compound without iso-surfaces (a) and with iso-surfaces (b).
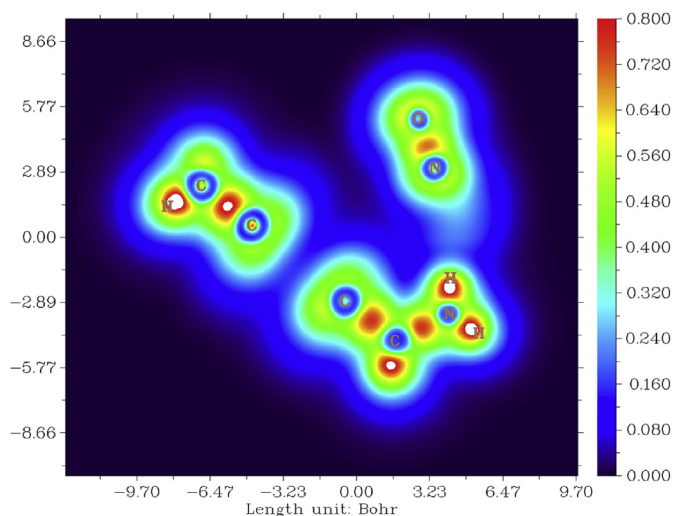
Figure 12. Localized orbital locator (LOL) map of 4MBN.

The ER_{XY} enrichment ratio of a chemical element pair (X, Y) is defined as the ratio of the percentage of actual contacts in the crystal to the theoretical percentage of random contacts. The enrichment ratios (ER) of the intermolecular contacts existing in the asymmetric unit are calculated and given in Table 5. The list of enrichment ratios highlights the O… H/ H… O contacts ($ER_{OH} = 1.2$) which appear to be favored in the crystal packing with the formation of N-H… O and C-H type … O hydrogen bonds of the. H … H contacts appear with an enrichment ratio close to unity (0.90), this value agrees well with Jlech's expectation [34]. Indeed these contacts necessarily occupy almost half of the (HS) with a percentage in SH> 70%. On the other hand, C … H/H … C contacts are slightly favored in a sample that contains aromatic molecules with an

average ER_{CH} value $= 1.41$. On the other hand, C… C contacts are in most cases very disadvantaged with RECC <0.5 [42].

3.2.3. Reduced density gradient method (RDG)

The reduced density gradient method (RDG) is also a most efficient technique for analyzing non-covalent interactions (NCI) [43]. This approach was developed by Johnson et al. [44] and it enables to identify and visualize zones of weak interactions in a molecular system, such as the van der Waals (VDW) interaction, hydrogen bonds (H-B) and steric effect. His expression is a dimensionless quantity coming from the density and its first derivative [43]:

$$RDG(r) = \frac{1}{2(3\pi^2)^{1/3}} \frac{|\nabla\rho(r)|}{\rho(r)^{4/3}} \tag{1}$$

The RDG represents a color code to examine the interaction within the systems molecular. Blue zone indicates the presence of strong attractive interactions ($\rho > 0$; $\lambda_2 < 0$), such as hydrogen bond, red zone indicates the presence of strong repulsive interactions ($\rho > 0$; $\lambda_2 > 0$), such as steric effect and green zone shows the presence of weak interaction ($\rho \approx 0$, $\lambda_2 \approx 0$) such as VDW interaction [45]. Showing the 2D and 3D RDG plots (Figure 15) proves that the blue isosurface located between the H atom and the O-H group indicates the presence of H-B. In three dimensional spaces (3D), the values of sign (λ_2) ρ allow to determine the nature of interactions. In fact, hydrogen bond (H-B) was located between -0.035 a.u < sign (λ_2) ρ < -0.020 a.u. The force between hydrogen atoms and NO_3 group is the VDW interaction (green isosurface). This region located between -0.015 a.u < sign (λ_2) ρ < -0.010 a.u. While, red color indicates the steric effect which is found in center aromatic rings (strong repulsion). These repulsive interactions were observed within 0.020 a.u < sign (λ_2) ρ < 0.035 a.u.

3.2.3.1. Independent gradient model (IGM) analysis. To visualize and quantify inter-intramolecular interactions a novel visible method independent gradient model (IGM) was carried out. This approach is based on promolecular density to identify the hydrogen bonding and van der
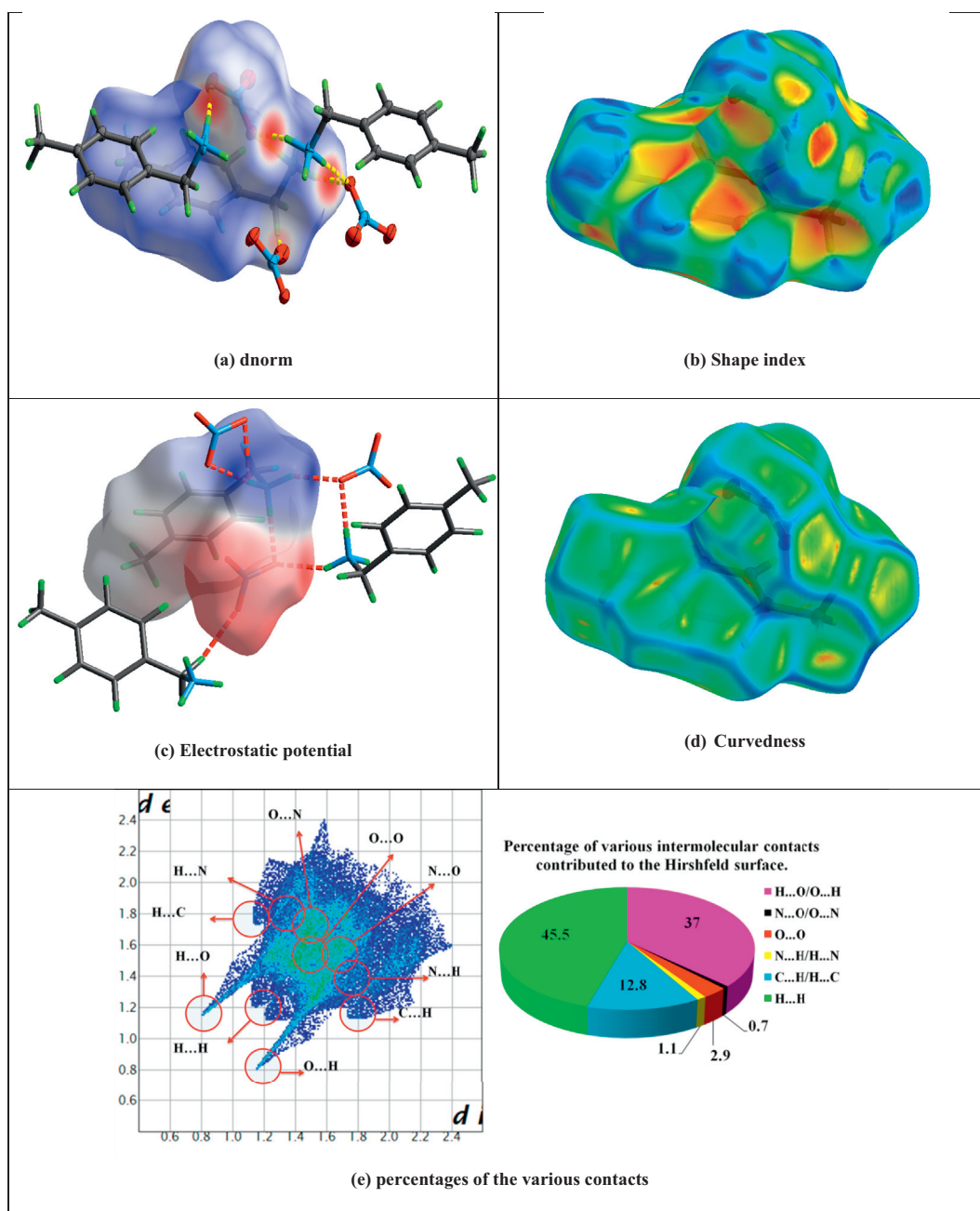
Figure 13. (a) "d_{norm}", (b) "Shape index", (c) electrostatic potential, (d) "Curvedness" and percentages of the various contacts of $(C_8H_{12}N)$ NO_3 mapped to the Hirshfeld surfaces.

Waals interaction presents in chemical systems. It also defined the independent gradient function (δg), the inter-fragment (δg^{inter}) and intra-fragment (δg^{intra}) to show interaction regions in the IGM. The multiwfn program was used to carry out the IGM analysis to reveal the non-covalent interactions (Figure 16) of our compound 4MBN [45]. This figure shows the range of δg values with an upper limit 0.2 (red color) and a lower limit is 0 (blue color). From this figure we see that the blue color around the carbon atoms indicates the charge depletion zone. Red color round hydrogen atoms present high electron density and the green color around the nitrogen atoms indicate the neuter zone. In addition, the white color indicates all chemical interactions that have bigger values of δg (a region with $\delta g > 0.2$). The plots which are presented by δg^{intra}, δg^{inter} and δg versus sign (λ_2) ρ values are depicted in Figure 17. Figure 17.a associated for inter-fragment (δg^{inter}) interactions indicates the presence of remarkable peak about 0.393 a.u with sign (λ_2) ρ is equal to -0.025.

The negative sign (λ_2) ρ implies attraction interaction (H-bond). The δg^{inter} shows also another low intensity peak about 0.098 a.u with sign (λ_2) ρ is equal to 0.035 a.u which indicates the presence of a repulsive interaction correspond to a steric effect. From the scattering plots of intra-fragment interaction (Figure 17.b), when sign (λ_2) ρ is equal to -0.035 a.u, the δg^{intra} has an intense peak which implies the presence of hydrogen bonds in our compound 4MBN. Two weak peaks are equal to 0.080 a.u and 0.050 a.u which are associated to sign (λ_2) $\rho \approx 0$ essentially corresponding to VDW interactions.

3.2.4. Natural orbital bond (NBO) analysis

NBO analysis is considered the most useful technique to describe and determine the different donor-acceptor interactions between the atoms of the studied molecular system. Its applies to study electronic transitions, charge transfer or hyper-conjugative interactions. It is also enables
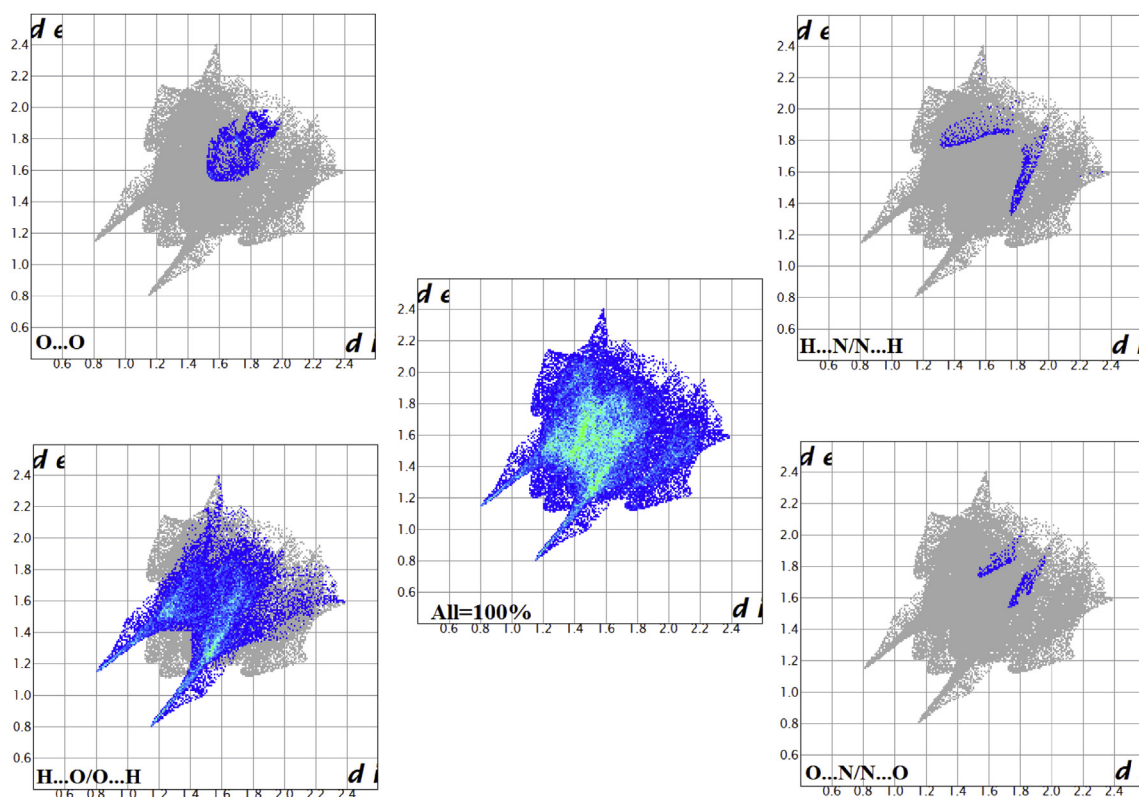
Figure 14. The fingerprint plots (d_i Vs d_e) of the title compound: (a) contact O...O, (b) H...O/O...H, (c) H...N/N...H, (d) O...N/N...O and (e) all intermolecular contact.

to identify the possible interactions between filled Lewis-type NBOs (donors) and Lewis unfilled NBOs (acceptors) for a molecule [46]. The stabilization energy of 2nd order E (2) related from any donor (i) and acceptor (j), can be estimated by the following equation [47].

$$E\,(2) = \Delta E_{IJ} = q_i\,F^{\,2}\,(i,\,j)\,/\,\varepsilon_j\text{-}\,\varepsilon_i \qquad (2)$$

where q_i is the donor occupancy, F (i, j) is the Fock matrix element, ε_i, ε_j are the diagonal elements of the orbital energies.

An NBO analysis was performed at the DFT level on the 4MBN structure optimized with the B3LYP/CC-PVTZ method. Table 6 enumerated the various interactions between Lewis (donor), non-Lewis (acceptor) orbits and second-order interaction energy E (2) $\geq$ 6 kcal/ mol corresponding to monomer and dimer. The greater E (2) values representing the high intensive interaction between electron donors and electron acceptors [48]. Referring to the results summarized in Table 6, it has noted the presence of strong interactions between electron-donors in the monomer and dimer. These interactions are formed by the orbital overlap between LP$_3$ (O$_4$) → Π*(N$_2$-O$_3$) and LP$_2$ (O$_1$) → Π*(N$_2$-O$_3$), of stabilizing energies E (2) equal to 151.79 kcal/mol and 41.01 kcal/mol respectively. In case of dimer, all interactions between Π*(C$_{36}$-C$_{41}$) → Π*(C$_{32}$-C$_{33}$) and Π*(C$_{30}$-C$_{35}$) → Π*(C$_{32}$-C$_{33}$) have high energy values equal to 261.74 kcal/mol and 158.28 kcal/mol respectively. The NBO analysis of 4MBN can clearly show the existence of hydrogen bonded interaction (N-H···...O) between nitrogen lone electron pairs (LP(N)) and σ*(O-H) anti-bonding orbital. The hyper-conjugated interaction energy between LP$_1$ (N$_5$) donor and σ*(O$_1$-H$_8$) acceptor is 45.70 kcal/mol. This hydrogen bonded interaction promotes the charge transfer in 4MBN and conserve the molecular stability. Hence, the monodentate coordination is clearly justified by this analysis. On the other hand, the study of bond orders, expressed as Wiberg bond index matrix in the NAO basis shows that of the two predicted hydrogen C15-H16···O1 and N5-H8···O1 bonds, suggested by AIM and Hirshfeld surfaces analyses, only one of them (N5-H8···O1) has a higher bond order value (0.5873), as compared with

the other one C15-H16···O1 (0.0019) justifying this way, the mono-dentate coordination by means of the N5-H8···O1 bond.

3.3. Electronic properties

3.3.1. Molecular electrostatic potential surface (MESP) analysis

In this part, surface of molecular electrostatic potential (MESP) is created to predict and analyzed the molecular reactive behaviour of a studied molecule. It is related to the electronic density and is a very useful to study hydrogen bonding interactions and for determining electrophilic and nucleophilic attack sites [49, 50]. The MESP map of 4MBN was constructed by using B3LYP/CC-PVTZ method and it mapped in Figure 18. The image of MESP was represented with color code located between two extremes: -4,671 10^{-2} (red indicates strongest repulsion) to 4,671 10^{-2} (blue indicates strongest attraction). Red regions represent the most appropriate sites for nucleophilic attack, blue region indicates sites for highest reactivity about electrophilic attack and green color corresponds to a neutral zone. Positive electrostatic potential (blue region) in 4MBN is found around NH$_3^+$ of the methylbenzylammouim cation group. Whereas, negative electrostatic potential (red and yellow regions) is localized around oxygen and nitrogen atoms of the NO$_3^-$ group. In addition, the electrophilic and nucleophilic sites explain the formation

Table 5. Enrichment ratio (RE) of the various contacts in (C$_8$H$_{12}$N) NO$_3$.

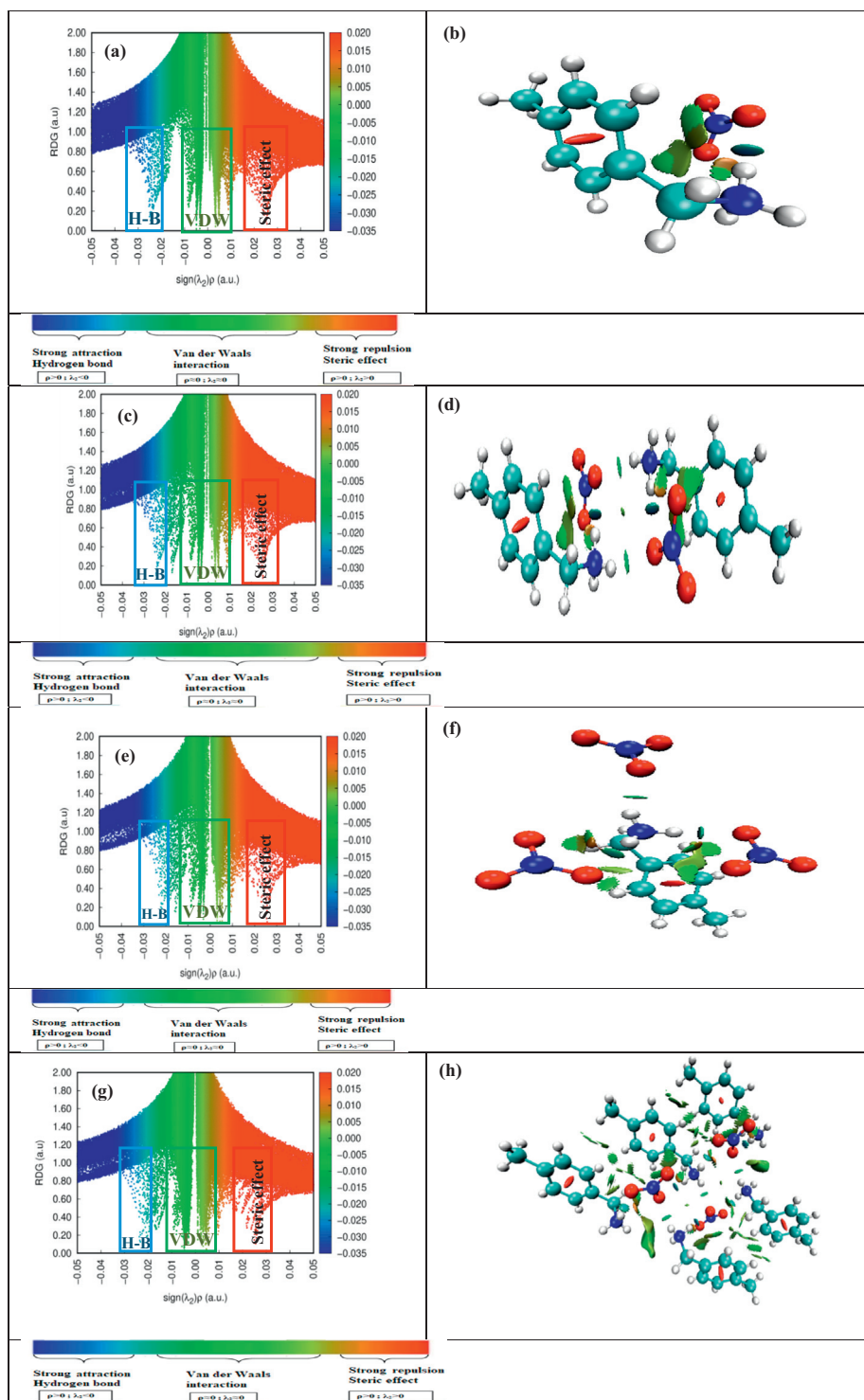| ER	H	C	N	O
H	0.90	1.41	0.86	1.2
C				
N				1.79
O				0.66
% Surface	70.95	6.4	0.9	21.75

Figure 15. 2D (left) and 3D (right) RDG plots of: (a), (b) monomer, (c), (d) dimer, (e), (f) around organic interaction, (g), (h) around inorganic interaction.

of hydrogen bonds between the nitrate groups and the methyl-benzylammouim and its importance in the stability of 4MBN.

3.3.2. Frontier molecular orbitals (HOMO-LUMO) analysis

Theory of frontier molecular orbital (FMOs) is an invaluable tool to discuss the energy transition of the charge density because these FMOs play a key role in optical, electrical and chemical properties of compounds [51, 52]. Thus, HOMO (electron donor) represents the highest occupied molecular orbital, while lowest unoccupied orbital LUMO (electron acceptor) that takes part in chemical stability [53]. These two bands describe the capacity of a molecule to offer an electron and to gain an electron respectively. Furthermore, HOMO-LUMO are energetically
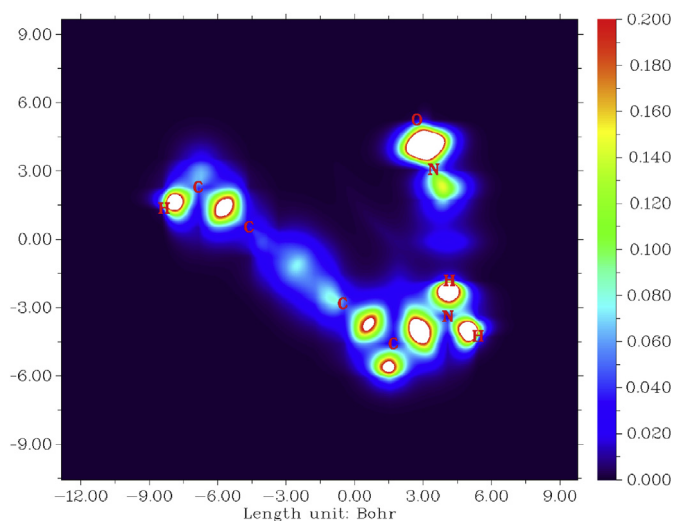
Figure 16. IGM graph of our compound 4MBN.

separated by an energy gap, also they plays an important role to characterize the chemical reactivity and chemical hardness-softness as well as optical polarizability of 4MBN [54]. Hence, the HOMO-LUMO plots of 4MBN were carried out in gas phase and in solvent effect (ethanol and water) which are given in Figure 19. As seen this figure, two important molecular orbital (MO) was examined which presented by two colors: green color represents negatively charged surfaces (nucleophilic sites), while red color indicates positively charged surfaces (electrophilic sites).

It is clear that the HOMO iso-density plots are located on $(C_8H_{12}N^+)$, while the LUMO iso-density plots are located on (NO_3). In addition, the global reactivity descriptors: global hardness (η), maximum load transfer index (ΔN_{max}), electronegativity χ and moment dipolar (μ) were defined by Parr R.G and colleagues [55]. Table 7 summarized these values, and indicates that the gap energies of 4MBN are equal to: 5.59 eV (gas), 4.04 (water) and 4.98 eV (ethanol). Since a compound with a higher-gap energy value is more polarizable, associated with high chemical reactivity, indicates low kinetic stability and is also called a soft molecule [56]. $\Delta N_{max} = 2.36$ eV is maximum in presence of water, which means that 4MBN acquires a maximum of charges in its structure unlike gas and ethanol. To examine the character of the molecular orbitals (MO) of our compound we have calculated the density of states (DOS) (Figure 20). It can be clearly seen from this figure that DOS spectrum shows two peaks in the presence of ethanol: one is very intense and well localized on LUMO orbital with energy equal to -0.89 eV, and other less intense localized on HOMO orbital with $E_{HOMO} = -6.2$ eV. In the gas phase, the two peaks HOMO and LUMO are less intense such that the energies $E_{HOMO} = -6.99$ eV and $E_{LUMO} = -1.41$ eV. In water, the band HOMO is located at $E_{HOMO} = -6.98$ eV and the band LUMO is located at $E_{LUMO} = -1.42$ eV. As well as their energy differences in ultimate value are equal to 5.91 eV, 5.61 eV, and 5.56 eV respectively in gas, ethanol and water. To know the contribution of each group, we have calculated the partial density of state (PDOS) as illustrated in the Figure 21. It can be observed from PDOS that in gas phase the two organic and nitrate groups are contributed to the bands HOMO and LUMO with $E_{HOMO} = -4.90$ eV and $E_{LUMO} = -1.10$ eV. Furthermore, the PDOS shows that under the effect of the solvent (water and ethanol) the two groups are assigned in the contribution of the HOMO-LUMO orbitals. The HOMO-LUMO energy is E_{HOMO} (ethanol) = -6.22 eV, E_{LUMO} (ethanol) = -0.51 eV and E_{HOMO}
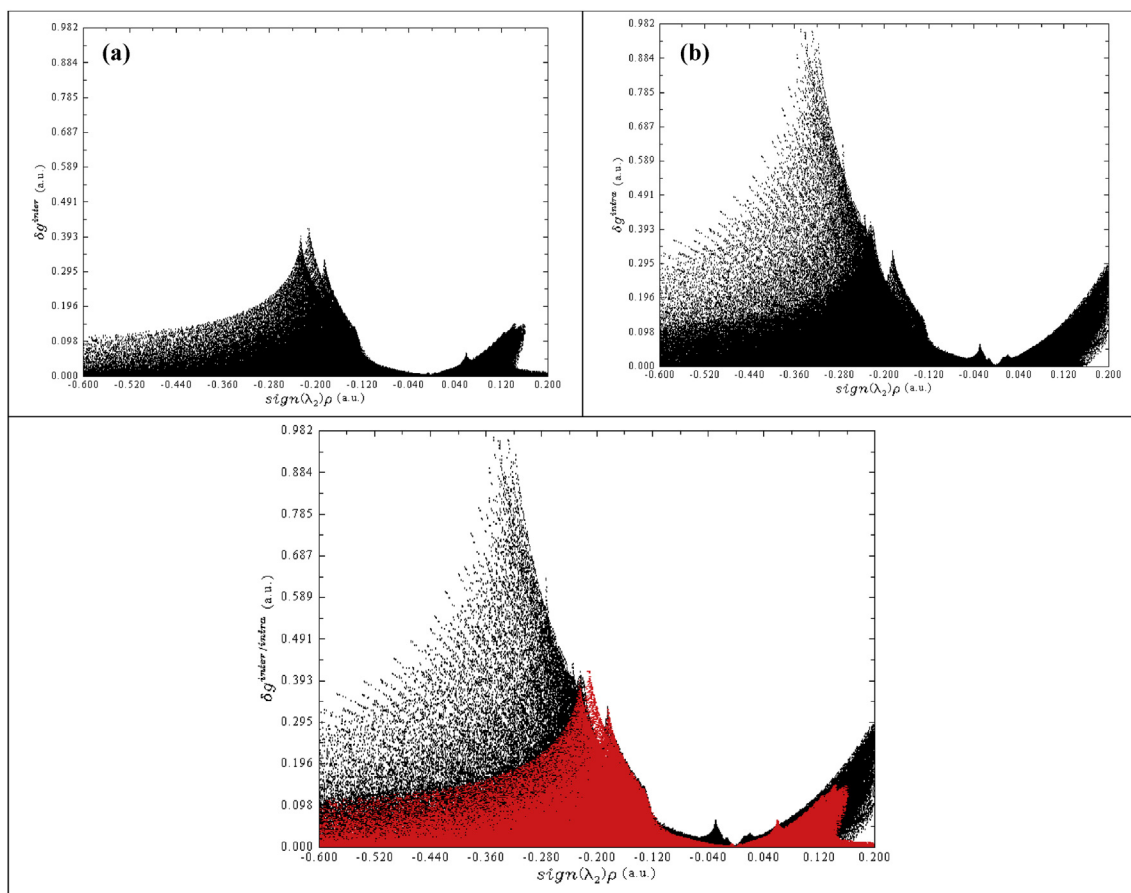

Figure 17. 2D-plots of IGM analysis: (a) sign $(\lambda_2)\rho$ Vs δg^{inter}, (b) sign $(\lambda_2)\rho$ Vs δg^{intra} and (c) sign $(\lambda_2)\rho$ Vs $\delta g^{inter/intra}$ (red and black color are related to δg^{inter} and δg^{intra}).

Table 6. Orbital analysis (NBO) of monomer and dimer from of 4-methylbenzy-lammouim nitrate compound.

Donor (i)	Acceptor (j)	E (2) kcal/mol	E(j)-E(i) a.u.	F (i. j) a.u.
Monomer				
π (N$_2$-O$_3$)	Π*(N$_2$-O$_3$)	9.69	0.34	0.061
LP$_1$(O$_1$)	σ*(N$_2$-O$_4$)	6.17	1.07	0.073
LP$_2$(O$_1$)	Π*(N$_2$-O$_3$)	41.01	0.20	0.093
LP$_2$(O$_3$)	σ*(O$_2$-N$_2$)	30.45	0.45	0.105
LP$_2$(O$_3$)	σ*(N$_2$-O$_4$)	18.55	0.70	0.104
LP$_2$(O$_4$)	σ*(O$_1$-N$_2$)	27.45	0.46	0.101
LP2(O$_4$)	σ*(N$_2$-O$_3$)	16.37	0.75	0.100
LP$_3$(O$_4$)	Π*(N$_2$-O$_3$)	151.76	0.15	0.141
LP$_1$(N$_5$)	σ*(O$_1$-H$_8$)	45.70	0.70	0.160
π (C$_9$-C$_{12}$)	Π*(C$_{11}$-C$_{20}$)	21.57	0.29	0.071
π (C$_9$-C$_{12}$)	Π*C$_{14}$-C$_{15}$	20.57	0.28	0.069
π (C$_{11}$-C$_{20}$)	Π*(C$_9$-C$_{12}$)	20.43	0.27	0.067
π (C$_{11}$-C$_{20}$)	Π*(C$_{14}$-C$_{15}$)	22.64	0.28	0.071
π (C$_{14}$-C$_{15}$)	Π*C9-C$_{12}$	21.74	0.28	0.070
π (C14-C15)	Π*(C$_{11}$-C$_{20}$)	19.56	0.29	0.067
Dimer				
π (N$_2$-O$_3$)	Π*(N$_2$-O$_3$)	14.23	0.32	0.074
LP$_2$ (O$_1$)	σ*(N$_2$-O$_3$)	16.45	0.70	0.096
LP$_2$(O$_1$)	σ*(N$_2$-O$_4$)	12.55	0.74	0.086
LP$_3$(O$_1$)	Π*(N$_2$-O$_3$)	89.40	0.18	0.124
LP$_2$(O$_3$)	σ*(O$_1$-N$_2$)	18.53	0.63	0.096
LP$_2$(O$_3$)	σ*(N$_2$-O$_4$)	16.69	0.70	0.097
LP$_2$(O$_4$)	σ*O$_1$-N$_2$)	19.22	0.65	0.099
LP$_2$(O$_4$)	σ*N$_2$-O$_3$)	18.79	0.67	0.101
LP$_3$(O$_4$)	Π*(N$_2$-O$_3$)	137.92	0.15	0.138
LP$_2$(O$_1$)	σ*(N$_5$-C$_8$)	6.55	0.84	0.067
σ (C$_9$-C$_{14}$)	σ*(N$_5$-C$_{17}$)	6.16	0.49	0.053
σ (C$_9$-C$_{14}$)	Π*(C$_{11}$-C$_{12}$)	16.99	0.31	0.064
σ (C$_9$-C$_{14}$)	Π*(C$_{15}$-C$_{20}$)	20.97	0.30	0.070
σ (C$_{11}$-C$_{12}$)	Π*(C$_9$-C$_{14}$)	24.13	0.27	0.072
σ (C$_{11}$-C$_{12}$)	Π*(C$_{15}$-C$_{20}$)	19.75	0.28	0.067
π (C$_{15}$-C$_{20}$)	Π*(C$_9$-C$_{14}$)	20.77	0.28	0.068
π (C$_{15}$-C$_{20}$)	Π*(C$_{11}$-C$_{12}$)	21.83	0.29	0.072
Π*(C$_9$-C$_{14}$)	Π*(C$_{11}$-C$_{12}$)	158.27	0.02	0.082
Π*(C$_{15}$-C$_{20}$)	Π*(C$_{11}$-C$_{12}$)	261.66	0.01	0.083
π (C$_{30}$-C$_{35}$)	π *(C$_{32}$-C$_{33}$)	16.99	0.31	0.064
π (C$_{30}$-C$_{35}$)	π *(C$_{36}$-C$_{41}$)	20.97	0.30	0.070
π (C$_{32}$-C$_{33}$)	π *(C$_{30}$-C$_{35}$)	24.13	0.27	0.072
π (C$_{32}$-C$_{33}$)	π *(C$_{36}$-C$_{41}$)	19.76	0.28	0.067
π (C$_{36}$-C$_{41}$)	π *(C$_{30}$-C$_{35}$)	20.77	0.28	0.068
π (C$_{36}$-C$_{41}$)	π *(C$_{32}$-C$_{33}$)	21.84	0.29	0.072
Π*(C$_{30}$-C$_{35}$)	π *(C$_{32}$-C$_{33}$)	158.28	0.02	0.082
Π*(C$_{36}$-C$_{41}$)	π *(C$_{32}$-C$_{33}$)	261.74	0.01	0.083
σ (N$_{48}$-O$_{49}$)	σ*(N$_{48}$-O$_{49}$)	14.24	0.32	0.074
LP2 (O$_{47}$)	Π *(N$_{48}$-O$_{49}$)	16.46	0.70	0.096
LP2 (O$_{47}$)	σ*(O$_{47}$-N$_{48}$)	12.55	0.74	0.086
LP3 (O$_{47}$)	σ*(N$_{48}$-O$_{50}$)	89.43	0.18	0.124
LP2 (O$_{49}$)	σ*(O$_{47}$-N$_{48}$)	18.53	0.63	0.096
LP2 (O$_{49}$)	σ*(N$_{48}$-O$_{50}$)	16.69	0.70	0.097
LP2 (O$_{50}$)	σ*(O$_{47}$-N$_{48}$)	19.22	0.65	0.099
LP2 (O$_{50}$)	σ*(O$_{47}$-N$_{48}$)	18.80	0.67	0.101
LP3 (O$_{50}$)	Π *(N$_{48}$-O$_{49}$)	137.92	0.15	0.138

🔹F (i. j) is the Fock matrix element between i and j orbits.

🔹E(j)-E(i) energy difference between acceptor (j) and donor (i) NBO orbits.

🔹E(2) energy of hyperconjugative interaction.

(water) = -6.80 eV, E$_{LUMO}$ (water) = -0.62 eV. From all these results we can conclude that our compound 4MBN is more reactive in water.

3.3.3. UV-visible spectroscopy

In order to understand the electronic transitions between the molecular orbits HOMO-LUMO in 4MBN, a TD-DFT calculation in the solvent ethanol was affected. UV-Visible absorption spectroscopy is an analytical method used to characterize a molecule, to find the nature of electronic transitions and oscillatory strength. The simulated and experimental UV-Visible absorption spectra of our compound in ethanol are shown in Figure 22. The effect of the solvent (ethanol) was taken into account by using the polarizable continuum model of the integral equation formalism (IEFPCM). The major absorption features: excitation energy E (eV), oscillator strength (f), wavelength λ (nm) and major contributions (%) of the molecular orbitals involved in each transition are reported in Table 8. In comparison with experimental study, UV-visible spectrum shows two peaks: the first is the most intense, located at λ_{max} = 277 nm (E = 4.48 eV) and 274 nm for spectra theoretical and experimental respectively is due to HOMO→LUMO transition with (97%) contribution. This electronic transition can be carried out at the Π→Π * transition relative to the organic group, due to the presence of the benzene ring. The second peak, was observed at $\lambda_{max \text{ (theoretical)}}$ = 235 nm (5.26 eV) and $\lambda_{max \text{ (experimental)}}$ = 307 nm corresponding to H-1→L+1, H-1→L+2, HOMO→L+1, HOMO→L+2 with (27%), (12%), (20%), (41%) contributions respectively. All these transition appear to be due to n →Π * of group nitrate.

3.4. Thermal behavior

The differential and thermogravimetric thermal analysis of 4-Methyl-benzylammonium nitrate is carried out in a temperature range from ambient up to 880 K on a sample of mass is equal to 10.2 mg with a heating rate of 5 K.min^{-1} and under an argon atmosphere. The DTA curve given in Figure 23. a shows the presence of an endothermic peak located at 397 K without loss of mass observed by TG curve. To better understand the nature of this phenomenon or of this transformation, the starting product was heated to a temperature slightly below 397 K for a few minutes, which causes the melting of our product and the start of its decomposition. A second exothermic peak is observed at 497 K. This peak is accompanied, on the TG curve, by a great loss of mass which corresponds to the total decomposition during which our compound undergoes an ignition and an explosion which leads to at the end of handling with nitrogen oxides [57, 58, 59]. The differential scanning calorimetry analysis (DSC) (Figure 23 b) of (4-CH$_3$C$_6$H$_4$CH$_2$NH$_3$)NO$_3$ compound is carried out under a stream of nitrogen using a Setaram "multimodule 92" type thermo-analyzer. This analysis is carried out on 11.21 mg of product placed in an alumina crucible from room temperature up to 535 K with a heating rate of 5 K. min^{-1}. The DSC analysis shows the presence of two peaks one endothermic located at 416 K and the other exothermic at 507 K corresponding respectively to the melting and decomposition of our product; these two phenomena are also observed by DTA/TG.

3.5. Vibrational study

The optimization of 4MBN with the B3LYP/CC-PVTZ method and the previous studies for this species have clearly evidenced the presence of NH$_3^+$ group belonging to methylbenzylammonium cation and the NO$_3^-$ group where the coordination mode is clearly monodentate. The experimental FT-IR spectrum of 4MBN in the solid phase was compared in Figure 24 with the corresponding predicted for the compound in the gas phase and with the Raman spectrum also predicted in the same medium and level of theory. The Raman spectrum predicted in activities was transformed to intensities with suggested equations [61, 62]. The complete assignments of 69 vibration modes expected for the structure of 4MBN with C_1 symmetry were carried out with the calculated harmonic
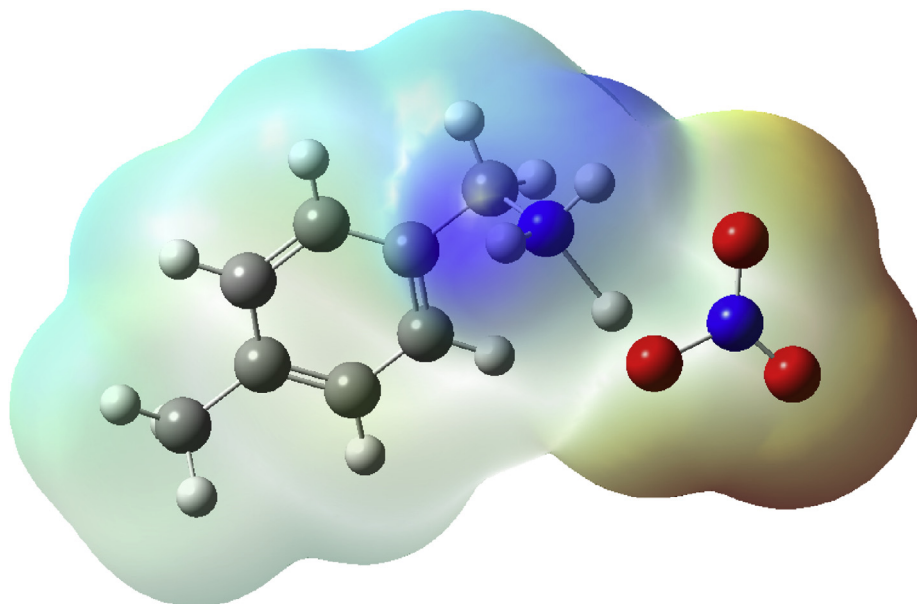
Figure 18. Molecular electrostatic potential map of the title compound.
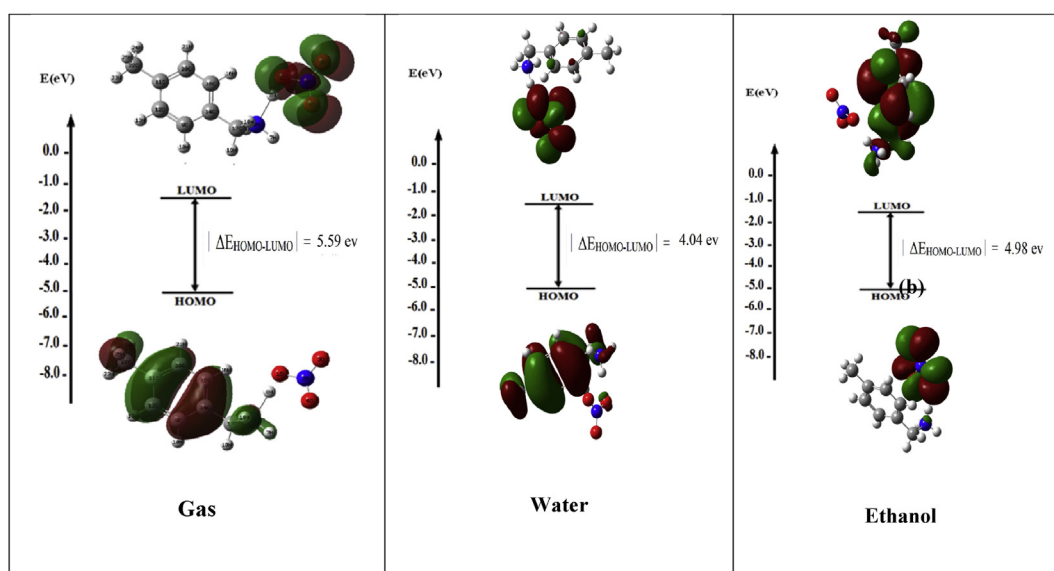

Figure 19. HOMO and LUMO molecular orbitals of 4MBN in gas phase, water and ethanol.

Table 7. HOMO-LUMO energy and other electronic properties of 4MBN compound.

DFT/B3LYP/CC-PVTZ	Gas	water	Ethanol
E_{HOMO} (ev)	-6.98	-6.78	-6.78
E_{LUMO} (ev)	-1.39	-2.74	-1.80
$\lvert \Delta E_{HOMO\text{-}LUMO} \rvert$ (ev)	5.59	4.04	4.98
Electronic affinity A (ev)	1.39	2.74	1.80
Ionization potential I (ev)	6.98	6.78	6.78
Electronegativity χ (ev)	4.19	4.76	4.29
Chemical potential μ (ev)	-4.19	-4.76	-4.29
Overall hardness η (ev)	2.79	2.02	2.49
Maximum load transfer index ΔN_{max} (ev)	1.50	2.36	1.72
Dipolar moment (Debye)	5.68	13.99	6.56
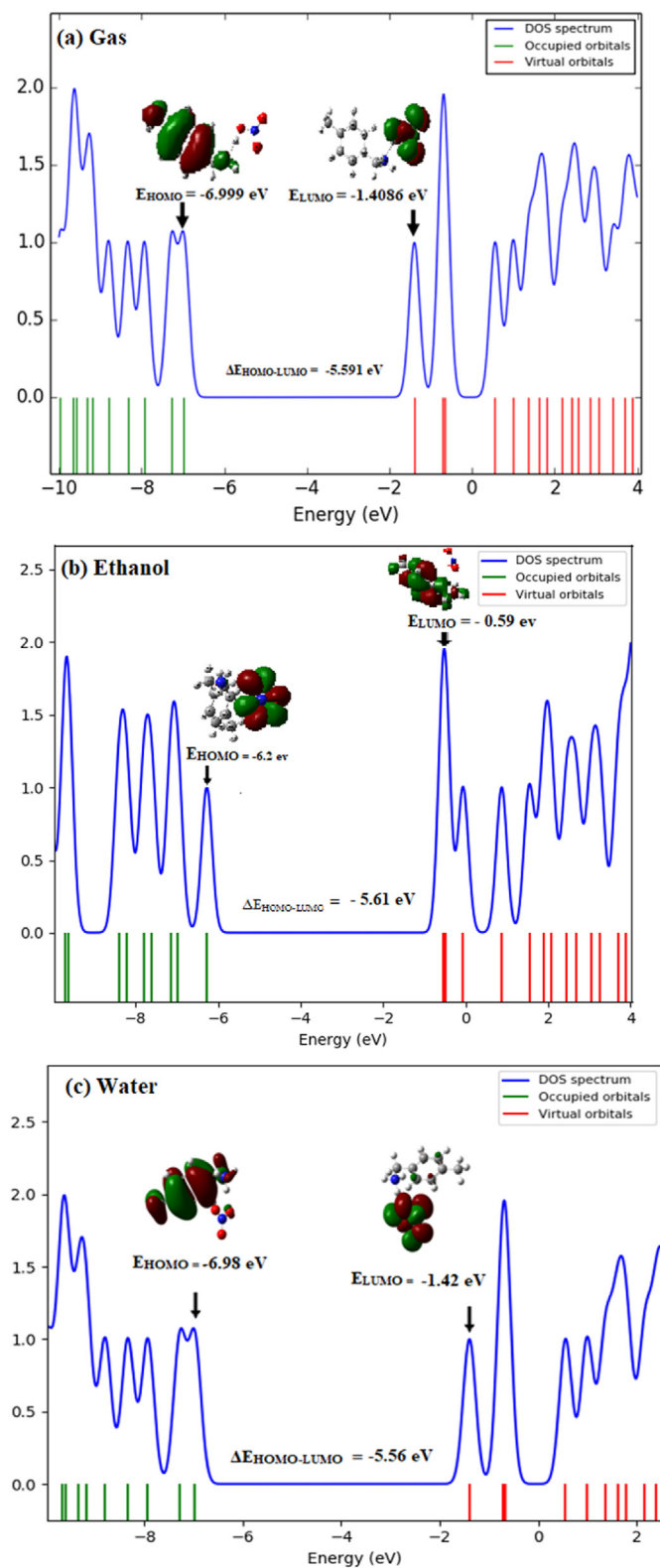
Figure 20. Density of stats (DOS) plots of 4MBN in: (a) gas, (b) ethanol and (c) water.

Figure 21. Partial density of stats (PDOS) plots of 4MBN in: (a) gas, (b) ethanol and (c) water.

force field in the gas phase by using the scaled quantum mechanical force field (SQMFF) methodology and taking into account the normal internal coordinates, transferable scaling factors and the Molvib program [16, 17, 18]. In the construction of the normal internal coordinates, as detailed in computational section, the NH_3 group was considered with C_{3V} symmetry while the NO_3 group with C_{2V} symmetry. In the assignments of all

vibrations modes were considered the SQM calculations performed here, potential energy distribution (PED) contributions ≥10 % and assignments reported for species with similar groups [5, 6, 7, 8]. Observed and

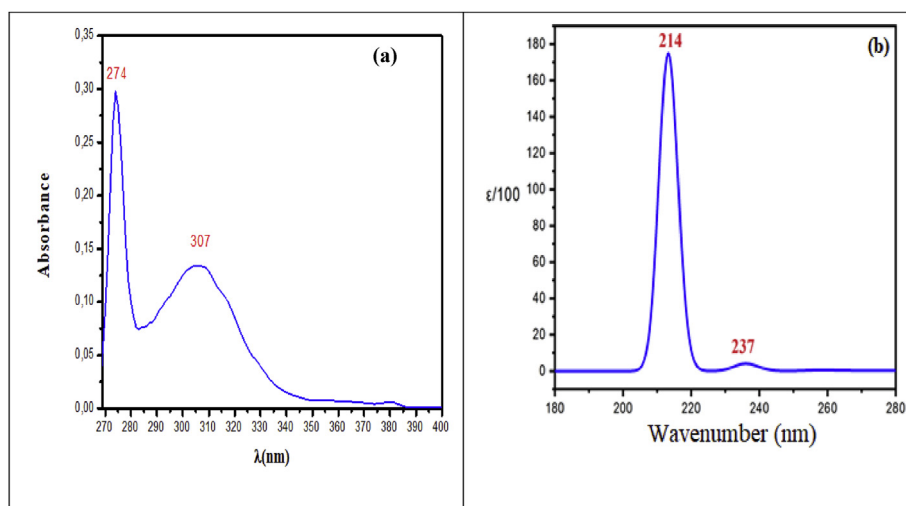**Figure 22.** UV-Visible spectrum: (a) experimental and (b) theoretical.

Table 8. Major absorption features: excitation energy (E). absorption wavelength (λ). oscillator force (f) and major contribution of the various electronic transitions.

E (ev)	λ (nm)	f (u. a)	Major contribution (%)
4.475	277.016	0.0002	HOMO→LUMO (97%)
4.677	265.048	0.0002	HOMO-3→LUMO (47%). HOMO-2→LUMO (36%). HOMO-1→LUMO (13%).
4.828	256.781	0.0003	HOMO-3→LUMO (14%). HOMO-1→LUMO (85%).
5.167	239.949	0.0002	HOMO-3→LUMO (37%). HOMO-2→LUMO (58%)
5.257	235.810	0.0026	HOMO-1→LUMO+1 (27%). HOMO-1→LUMO+2 (12%). HOMO→LUMO+1 (20%). HOMO→LUMO+2 (41%)
5.814	213.247	0.1167	HOMO-1→LUMO+2 (16%). HOMO→LUMO+1 (51%). HOMO→LUMO+2 (22%).

calculated wavenumbers for 4MBN in the gas phase by using B3LYP/CC-PVTZ calculations together with the corresponding assignments can be seen in Table 9. Note that the intense IR band predicted with the B3LYP/CC-PVTZ method at 2492 cm^{-1} and by SQM calculations at 2390 cm^{-1} is quickly assigned by its intensity to the N-O···H stretching mode of acid coordinate to NH$_2$ group, as was reported for the p-xylylenediaminium bis(nitrate) at 2651 cm^{-1} [6]. Thus, the experimental IR bands between 2615 and 2346 cm^{-1} (with red circle in Figure 13) can be assigned to O1-H8 stretching mode although the intensity of band in the

experimental spectrum is different from the theoretical one probably due to that the dimeric species is also present in the solid phase, as was reported for p-xylylenediaminiumbis (nitrate) [6]. Discussions of some assignments for the most important groups are presented below.

3.5.1. Assignments

3.5.1.1. NH$_3$ $^+$ groups.
In 4MBN, the N5-H8 bond is coordinate to OH group of acid and, for this reason, this bond present different
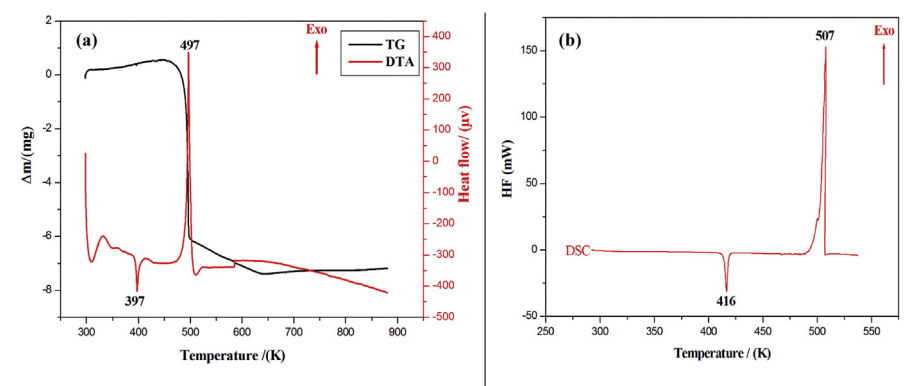

Figure 23. (a) DTA curve and (b) differential scanning calorimetry analysis (DSC) of 4MBN.
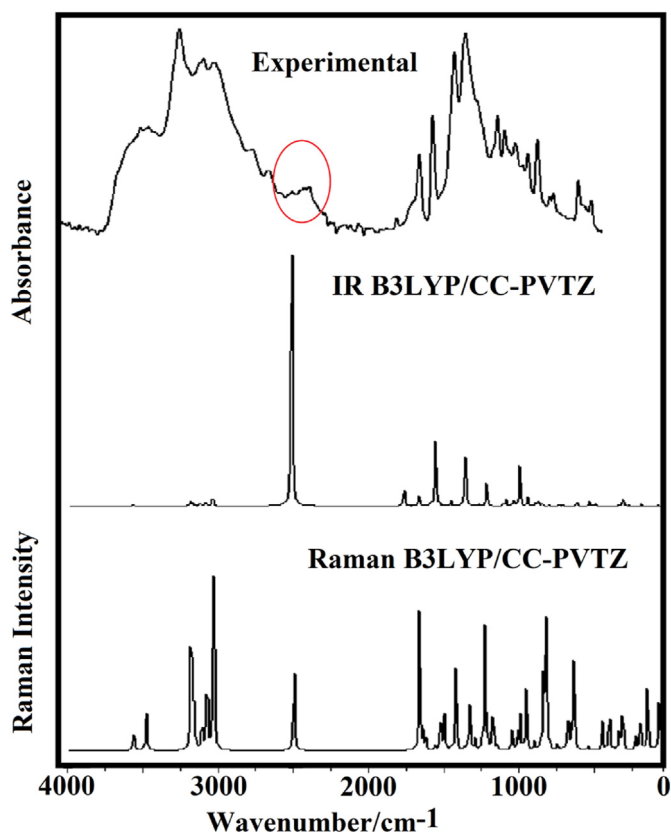
Figure 24. Theoretical and experimental FT-IR and Raman spectrum of 4MBN.

characteristic than the other two N5-H6 and N5-H7 ones. Many theoretical studies show that this mode are more sensitive to the presence of the hydrogen bond [63, 64, 65]. Hence, an anti-symmetric stretching mode of this group is predict at 3408 cm^{-1} while the other one at 251 cm^{-1} due to the coordination with the H8 atom of acid. The corresponding symmetric mode is predicted at 3329 cm^{-1}. Hence, these NH$_3$ stretching modes are assigned in different positions. The coordinate N$\cdots$H bonds in p-xylylenediaminiumbis (nitrate) are predicted between 271 and 119 cm^{-1} [6]. The anti-symmetric and symmetric deformation modes corresponding to these groups in the dimer of p-xylylenediaminiumbis (nitrate) [6] are predicted between 1793 and 1639 cm^{-1} while for the monomer between 1597 and 1591 cm^{-1}. In 4MBN, both anti-symmetric and symmetric deformation modes are predicted at 1565 cm^{-1} while the other anti-symmetric mode due to the coordination appears at 435 cm^{-1}. In p-xylylenediaminium bis(nitrate) [6], the rocking modes of these groups due to the monodentate coordination are predicted in the lower wavenumbers region. Here, these modes are predicted at 1144 and 51 cm^{-1} while the twisting mode is predicted coupled with other vibration modes between 489 and 448 cm^{-1}. In the dimer of p-xylylenediaminium bis(nitrate) this modes is assigned between 476 and 419 cm^{-1} while for the monomeric species these modes are predicted around 30 cm^{-1} [6].

3.5.1.2. Nitrate groups. In 4MBN, two N=O and one N-O stretching modes are expected due to the monodentate coordination of N-O$\cdots$H bond. In some inorganic nitrate salts, the N=O stretching modes are observed between 1672 and 1460 cm^{-1} [66,67], in niobyl nitrate are assigned between 1763 and 1753 cm^{-1} [68] while in species containing NO$_2$ groups these modes are assigned between 1584 and 1335 cm^{-1} [5, 69]. Here, due to the monodentate coordination the very strong band at 1305 cm^{-1} is clearly assigned to symmetric mode because the SQM calculations predict this mode at 1277 cm^{-1} while the anti-symmetric mode is assigned to the shoulder at 1652 cm^{-1} because this mode is

Table 9. Observed and calculated wavenumbers (cm^{-1}) and assignments for 4-methylbenzylammonuim nitrate in gas phase by using the B3LYP/CC-PVTZ method.

4-methylbenzylammonuim nitrate

Experimental[a]	B3LYP/CC-PVTZ Method[a]			
IR	Calculated[b]	Intensity[c]	SQM[d]	Assignments[a]
3468w	3555	8.4	3408	ν_aNH$_3$
3414w	3473	1.9	3329	ν_sNH$_3$
3207vs	3179	3.5	3048	νC15-H16
3048s	3171	21.9	3040	νC12-H13
3035sh	3160	8.8	3029	νC20-H21
3020w	3153	11.5	3022	νC9-H10
2978s	3104	15.8	2976	ν_aCH$_3$
2943sh	3075	15.9	2948	ν_aCH$_3$
2948sh	3066	14.1	2939	ν_aCH$_2$
2902sh	3026	25.8	2901	ν_sCH$_3$
2842sh	3021	35.0	2896	ν_sCH$_2$
2615/2346	2492	2315.9	2390	νH8-O1
1652sh	1736	152.7	1683	τH8-N5.τO1-H8. ν_aNO$_2$
1609m	1659	4.5	1605	νC15-C20.νC9-C12
1522s	1634	57.9	1565	δ_aNH$_3$. δ_sNH$_3$
1522s	1616	0.6	1563	νC11-C12.νC9-C14.νC14-C15
1507sh	1554	13.4	1506	βC15-H16
1465sh	1526	388.0	1470	τH8-N5.τO1-H8
	1517	11.9	1449	δCH$_2$
	1498	12.0	1437	δ_aCH$_3$
1425sh	1490	6.5	1426	δ_aCH$_3$
	1449	3.8	1403	δ_aCH$_3$. wagCH$_2$
1379s	1419	12.4	1393	wagCH$_2$
	1418	16.7	1356	δ_sCH$_3$
1322sh	1360	0.9	1325	βC12-H13.βC20-H21
1305vs	1337	3.3	1293	νC11-C20
1305vs	1324	431.3	1277	ν_sNO$_2$
1234sh	1290	5.1	1241	ρCH$_2$
	1244	1.2	1212	νC14-C17
1199sh	1228	5.3	1183	νC11-C22
1168sh	1215	2.1	1180	βC9-H10
	1182	123.0	1144	ρ'NH$_3$
1120sh	1171	7.0	1130	τH8-N5.τO1-H8
1092m	1146	1.5	1111	νC9-C12.βC12-H13
1044w	1067	6.5	1043	ρ'CH$_3$
1021sh	1049	31.0	1023	βR$_1$
1000vw	1043	1.1	1002	τH8-N5.τO1-H8
983sh	1012	4.4	987	γC15-H16
973w	997	1.3	981	ρCH$_3$
966sh	994	23.7	964	γC9-H10.γC12-H13
966sh	973	2.6	953	νC17-N5
923w	958	207.2	930	νN2-O1
888w	905	45.4	852	γC20-H21
888w	863	3.7	851	τwCH$_2$
826m	846	24.1	822	τH8-N5.τO1-H8
806sh	829	23.1	807	βR$_3$
743w	804	11.2	794	wagNO$_2$
715w	759	4.5	739	τR$_1$
705sh	722	0.2	700	τR$_1$.τR$_2$
681vw	693	3.7	681	δNO$_2$.τH8-N5
646vw	665	3.8	656	ρNO$_2$
	659	0.5	653	βR$_2$
555w	573	19.8	564	δC14C17N5
467w	489	22.3	477	γC11-C22. τwNH$_3$

(*continued on next page*)

Table 9 (*continued*)

4-methylbenzylammonuim nitrate

Experimental[a]	B3LYP/CC-PVTZ Method[a]			
IR	Calculated[b]	Intensity[c]	SQM[d]	Assignments[a]
432sh	449	16.5	435	$\delta_a NH_3$
403vw	421	0.6	407	$\tau R_3.\tau R_2.\tau wNH_3$
	388	1.0	384	$\beta C11-C22$
	369	0.6	363	$\tau H8-N5.\tau O1-H8$
	291	1.8	287	$\beta C14-C17$
	261	59.9	251	$\nu_a NH_3$
	218	1.7	213	$\tau H8-N5.\tau O1-H8$
	139	7.0	130	$\tau H8-N5$
	109	1.6	105	$\tau O1-H8.\nu_a NH_3$
	88	1.0	83	$\tau H8-N5.\tau O1-H8$
	54	0.2	51	$\rho NH_3.\delta N5H8O1.\tau C14-C17.\tau wNO_2$
	44	0.3	39	τwCH_3
	36	0.6	33	$\tau O1-H8.\tau H8-N5$
	27	0.7	24	$\tau O1-H8.\tau H8-N5$
	23	1.3	21	$\tau O1-H8$

Abbreviations: ν. stretching; β. deformation in the plane; γ. deformation out of plane; τ. torsion; β_R. deformation ring τ_R. torsion ring; ρ. rocking; τw. twisting; δ. deformation; wag. wagging; a. antisymmetric; s. symmetric; (A₁). Ring 1; [a]This work. [b]From B3LYP/CC-PVTZ method. [c]Intensities in KM/Mole; [d]From scaled quantum mechanics force field.

Table 10. Comparison of main scaled internal force constants for 4-methylbenzy-lammonuim nitrate in gas phase by using the B3LYP/CC-PVTZ method with reported for monodentate coordinations of p-xylylenediaminium bis(nitrate) and chromyl nitrate with different basis set.

B3LYP Method

	4-Methylbenzylammonuim nitrate[a]	p-Xylylenediaminium bis(nitrate)[b]	Chromyl nitrate[c]
Force constant	CC-PVTZ	6-311++G**	6-311++G
$f(\nu N = O)$	9.75	9.74	15.83
$f(\nu N-O)$	4.29	4.25	3.22
$f(\nu C-N)$	4.20	4.23	
$f(\nu C-C)$	4.30	4.27	
$f(\nu C-C_R)$	6.35	6.34	
$f(\nu N-H_3)$	4.37	4.36	
$f(\delta O = N=O)$	1.54	1.53	1.58
$f(\delta O = N-O)$	1.60	1.58	2.09
$f(\delta N-O-H)$	1.12	0.89	
$f(\delta N-H-O)$	0.18	0.19	

Units are mdyn Å^{-1} for stretching and mdyn Å rad^{-2} for angle deformations. [a]This work. [b]From Ref. [6]. [c]From Ref. [63].

coupled with the $\tau H8-N5$ and $\tau O1-H8$ torsion modes. The stretching mode related to simple N2-O1 bond is predicted at 930 cm^{-1} and, for this reason, the weak band at 923 cm^{-1} is assigned to this vibration mode. The O=N=O deformation mode is predicted and assigned at 681 cm^{-1} while the wagging and rocking modes are assigned at 743 and 686 cm^{-1}, respectively The torsion modes for the monodentate form of p-xylyle-nediaminiumbis (nitrate) [6] are predicted at 76 cm^{-1} while in 4MBN this mode is predicted at 51 cm^{-1}, as indicated in Table 9.

3.5.1.3. CH₃ and CH₂ groups. 4MBN has one CH₃ and CH₂ groups, later; the corresponding anti-symmetric and symmetric stretching modes are

predicted between 2976 and 2896 cm^{-1} and, for these reasons, the shoulders and group of IR bands in that region are assigned to these vibration modes, as is detailed in Table 9 [6, 7, 8, 69]. The symmetries of these modes cannot be verified because in this work the Raman spectrum was not recorded. The deformation modes of these groups are predicted between 1449 and 1356 cm^{-1} while the wagging CH₂ and rocking CH₃ modes are predicted at 1403/1393 and 1043/981 cm^{-1}, respectively. The SQM calculations predicted the twisting CH₂ mode at 851 cm^{-1} whiles the corresponding to CH₃ group at 39 cm^{-1}. This way, only the twisting CH₂ mode is assigned at 888 cm^{-1}.

3.5.1.4. Skeletal groups. The C=C stretching modes corresponding to the benzyl rings of p-xylylenediaminium at 1622 cm^{-1}, as reported in other similar compounds [5, 6, 8] while in 4MBN are predicted between 1605 and 1563 cm^{-1}. Hence, these modes are assigned to the IR bands at 1609 and 1522 cm^{-1}. On the other hand, the C-C stretching modes are predicted by SQM calculations between 1293 and 1111 cm^{-1} while the C-N stretching mode is predicted at 953 cm^{-1} and assigned to the shoulder at 966 cm^{-1}. The deformation and torsion of benzyl ring are assigned in the expected 1000-200 cm^{-1} region, as predicted by SQM calculations [5, 6, 8, 69].

3.6. Force constants

The harmonic force constants are interesting and useful parameters to analyze the forces of different bonds and, especially when the molecule under study presents monodentate coordination as in 4MBN. These constants were calculated for 4MBN in the gas phase from the harmonic force field with the SQMFF methodology and by using B3LYP/ CC-PVTZ method and the Molvib program [16, 17, 18]. The scaled force constants for 4MBN in the gas phase are compared in Table 10 with reported for species with monodentate coordinations, such as p-xylyle-nediaminium bis(nitrate) [6] and chromyl nitrate [67]. These comparisons are interesting because these compounds present the same coordination modes but different chemical characteristics, thus p-xyly-lenediaminium bis (nitrate) is a hybrid as 4MBN [6] while chromyl nitrate is an inorganic compound [67]. Comparing first the constants for both hybrid species we observed practically the same values for the two species and only slight changes in the $f(\delta N-O-H)$ force constants values are observed. Such differences could be attributed in part to the different basis sets used in the calculations. When the $f(\nu N = O)$ and $f(\nu N-O)$ force constants values for 4MBN are compared with the corresponding to chromyl nitrate we observed that the $f(\nu N = O)$ force constant value is lower in 4MBN while the other $f(\nu N-O)$ force constant is lower in chromyl nitrate [67]. Obviously, these differences are quickly associated to different nature of atoms linked to NO₃ group because in chromyl nitrate this group is coordinated to Cr while in 4MBN is co-ordinated to H. Hence, the Cr atom is most electropositive than H and, for this reason, the coordination is stronger between Cr and O (Cr←O) than H and O (H←O) [67].

3.7. Molecular docking

With the development of computer tools in the last 20 years, molecular docking is becoming a very efficient tool for the determination of biological activities. The docking study is a critical step in understanding biological reactions and in drug design [54, 55, 56, 57, 58, 59]. The objective of the computational molecular docking was performed to find out the orientations in space and bonding conformations between ligands with the target receptor [58]. A bibliographic study shows that the protein amino acid oxidase (DAO) is usually used in the treatment of mental disorder. In this study, docking calculations was effected for targeted protein related to the treatment of schizophrenia. The prototypical DAO inhibitor has been shown to be
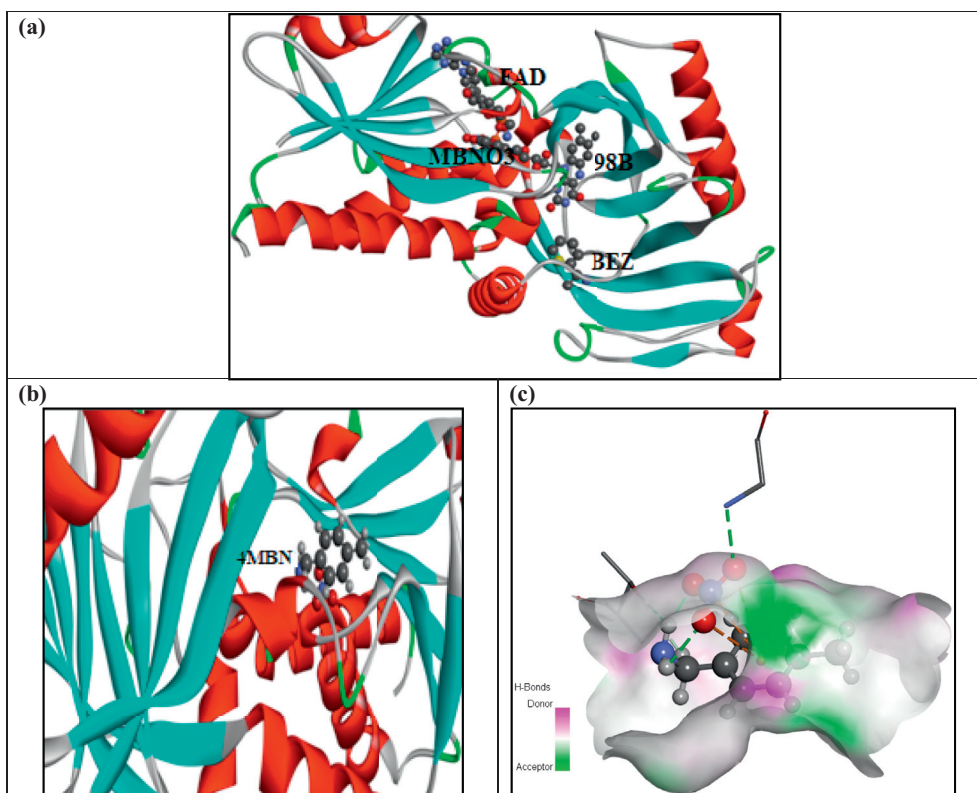
Figure 25. (a), (b) and (c) graphs of the best pose of 4MBN in the DAO protein.

effective in improving neurocognitive symptoms [60] and in the treatment of this disease [61, 62]. Molecular docking was used to evaluate the activity of quarter ligands: 4MBN, BEZ, FAD and 98B described in the literature as potential inhibitors of DAO. These ligands and protein structures are extracted from the PDB (Protein Data Bank) [14]. This database contains thousands of protein structures obtained either by crystallography (X-ray) or by NMR.

Figure 25 and Figure 26 show the best pose which corresponds to the minimum energies of the ligands in the DAO protein and 2D interactions between the different complexes gained from the docking of all studied ligands inside DAO. The total energy, VDW interactions, electronics and H-bond values obtained are indicated in Table 11. As reported clearly in this table that the predominant interaction is of VDW type. DAO-FAD complex showed the highest total energy (-304.288 Kcal/mol), with interaction energies of the order of: E_{VDW} = -232.615 kcal/mol, $E_{H\text{-}bond}$ = -71.272 kcal/mol and $E_{electronic}$ = -0.400 kcal/mol. The total energy scores of 4MBN, 98B and BEZ are respectively equal to: -76,828 kcal/mol, -65,111 kcal/mol and -61,792 kcal/mol, respectively. As depicted in Figure 25, all three ligands have almost the same positions in the protein. Their VDW interactions are of the order of -50.987 kcal/mol, -58.135 kcal/mol and -47.198 kcal/mol, as well as their hydrogen bond energies are equal to -25.841 kcal/mol, -6.976 kcal/mol and -14,594 kcal/mol, respectively. In another important steps Figure 10. C and Figure 27 show the presence of several types of interactions such as: Pi-alkyl, Pi-anion, hydrogen bonds and conventional hydrogen interactions which exist between the ligands and residues. In fact, electron acceptor-donor interactions promote the formation of these bonds. Therefore, these interactions mediate the stabilization of the complex with the residues (inhibitor stability).

Molecular docking studies have evidenced that 4MBN penetrates well into the active sites of the receptor while the interactions observed between the DAO protein and the 4MBN ligands prove a good degree of inhibition against schizophrenia disease.

4. Conclusions

In this research, the hybrid 4MBN compound has been synthesized in order to study the influence of non-covalent interactions on its experimental infrared spectrum and on its structural, electronic, topological and vibrational properties. For these purposes, the experimental IR spectrum and the structure previously determined by X-ray diffraction were employed in combination with B3LYP/CC-PVTZ level of theory to optimize 4MBN in gas phase and in ethanol and aqueous solutions. Then, the complete vibrational assignments of 69 vibration modes expected for the most stable structure of 4MBN was performed by using the SQMFF methodology together with the normal internal coordinates and scaling factors. Different computational and analytical methods, such as AIM, RDG, Hirsfeld surface analysis, NBO, MEP surfaces were used to describe the non-covalent interactions in 4MBN. The AIM analysis of topological parameters and Hirsfeld surfaces have showed the presence of two weak hydrogen bonds (N-H···O and C-H···O) in 4MBN while the study of bond orders support the higher value of N-H···O interaction. Hence, the monodentate coordination between cation and anion is also supported by the predicted strong IR band assigned to the N-O···H stretching mode of acid coordinate to NH_2 group of 4MBN. The RDG reduced density gradient method makes it possible to demonstrate, in addition to hydrogen bonds, the presence of van der Waals-type interactions and the steric effect. Natural orbital analysis (NBO) has shown that LP (O) → σ * (O-H) interactions (hydrogen bonds) stabilize the structure. Likewise, electronic properties were performed using the TD-DFT method. The nucleophilic and electrophilic sites were identified by calculating the Molecular Electrostatic Potential Surface (MESP). They clearly explain the monodentate coordination between nitrate and methylbenzylammonium groups and its importance in the stabilization of 4MBN. The Frontier Molecule Orbital Analysis (FMOs) of 4MBN in ethanol and aqueous solutions suggest that this species is most reactive in water. The UV-Visible spectra were studied
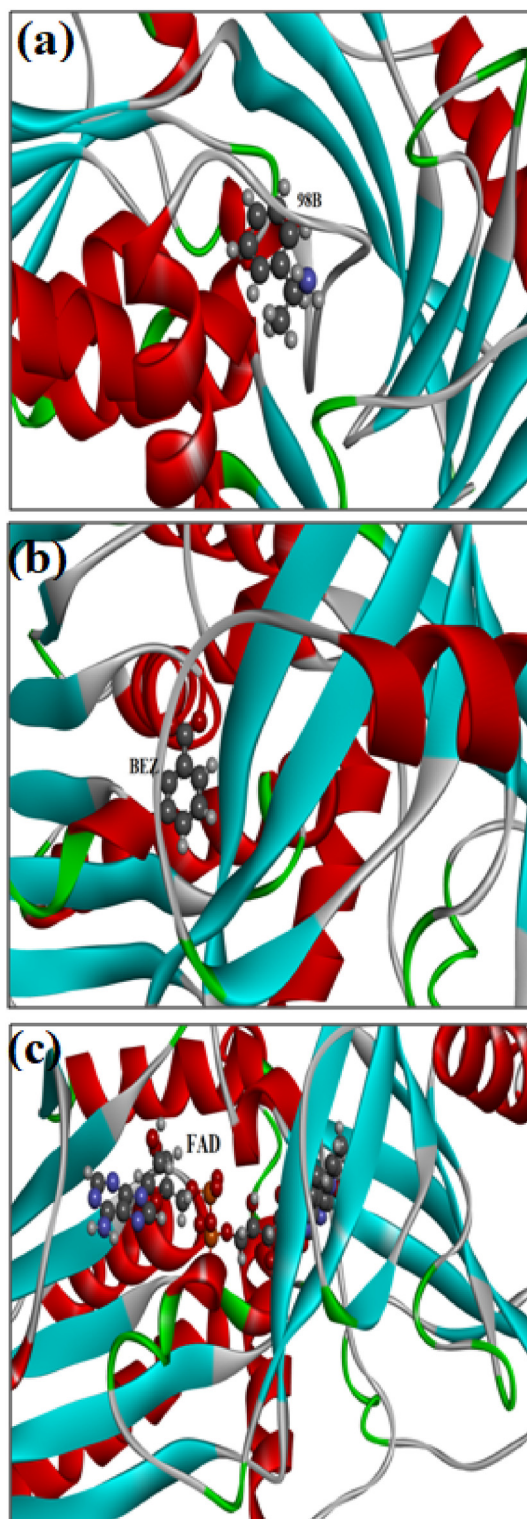
Figure 26. Best pose of (a) BEZ, (b) 98B and (c) FAD in the DAO protein.

Table 11. Docking calculation in DAO protein.

Protein	Ligand	Total energy	VDW	H-bond	Electronic
DAO	FAD	-304.288	-232.615	-71.272	-0.400
	4MBN	-76.828	-50.987	-25.841	0
	98B	-65.111	-58.135	-6.9759	0
	BEZ	-61.792	-47.198	-14.594	0
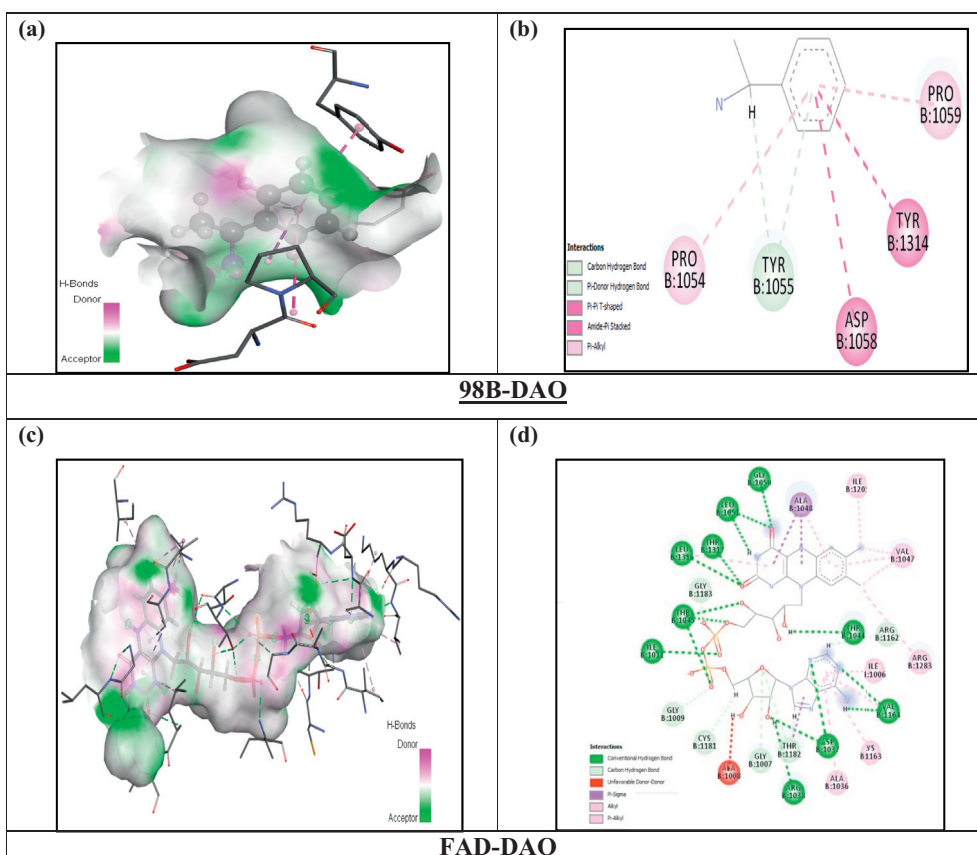
Figure 27. Representation of H-bond interactions between DAO protein and ligands. In the left: (a) 98B ligand, (c) FAD ligand. In the right: 2D diagram of (b) 98B-DAO and (d) FAD-DAO complexes.

by both experimental and DFT calculation in ethanol. Finally, molecular docking reveals that the title compound could act as an inhibitor against schizophrenia disease.

Declarations

Author contribution statement

Mouna Medimagh; Silvia Antonia Brandán: Analyzed and interpreted the data; Wrote the paper.

Noureddine Issaoui; Omar Al-Dossary: Conceived and designed the analysis.

Sofian Gatfaoui: Performed the experiments; Conceived and designed the experiments; Contributed reagents, materials, analysis tools or data.

Houda Marouani: Conceived and designed the experiments; Contributed reagents, materials, analysis tools or data.

Marek. J. Wojcik: Conceived and designed the experiments; Analyzed and interpreted the data.

Data availability statement

The authors do not have permission to share data.

Declaration of interests statement

The authors declare no conflict of interest.

Additional information

No additional information is available for this paper.

References

[1] C. Kashyap, S.S. Ullah, L.J. Mazumder, A.K. Guha, Non-covalent interaction in benzene and substituted benzene: a theoretical study, Comput. Theor. Chem. 1130 (2018) 134–139.

[2] M. Vimala, S.S. Mary, R. Ramalakshmi, S. Muthu, A. Irfan, Computational prediction of polar and non-polar solvent effect on the electronic property of N-BOC-Piperidine-4-Carboxylic acid, J. Mol. Liq. 341 (2021) 117222.

[3] S. Gatfaoui, H. Marouani, M. Rzaigui, 4-Methylbenzylammonium nitrate, Acta Crystallogr. Sect. E: Struct. Rep. Online 69 (9) (2013) o1453-o1453.

[4] L.S. Èder, D.J. Watkin, A. Cousson, Richard Ian Cooperb, Werner Paulusc, CRYSTALS enhancements: refinement of atoms continuously disordered along a line, on a ring or on the surface of a sphere, J. Appl. Crystallogr. 37 (2004) 545–550.

[5] M.V. Castillo, R.A. Rudyk, L. Davies, S.A. Brandan, Analysis of the structure and the FT-IR and Raman spectra of 2-(4-nitrophenyl)-4H-3,1-benzoxazin-4-one. Comparisons with the chlorinated and methylated derivatives, J. Mol. Struct. 1140 (2017) 2–11.

[6] S. Gatfaoui, N. Issaoui, S.A. Brandán, T. Roisnel, H. Marouani, Synthesis and characterization of p-xylylenediaminiumbis(nitrate). Effects of the coordination modes of nitrate groups on their structural and vibrational properties, J. Mol. Struct. 1151 (2018) 152–168.

[7] J. Kausteklis, V. Aleksa, M.A. Iramain, S.A. Brandán, Cation-anion interactions in 1-buthyl-3-methyl imidazolium nitrate ionic liquid and their effect on their structural and vibrational properties, J. Mol. Struct. 1164 (2018) 1–14.

[8] S. Gatfaoui, A. Sagaama, N. Issaoui, T. Roisnel, H. Marouani, Synthesis, experimental, theoretical study and molecular docking of 1-ethylpiperazine-1,4-diium bis(nitrate), Solid State Sci. 106 (2020) 106326.

[9] Gaussian 09, Revision C.01, M.J. Frisch, G.W. Trucks, H.B. Schlegel, G.E. Scuseria, M.A. Robb, J.R. Cheeseman, G. Scalmani, V. Barone, B. Mennucci, G.A. Petersson, H. Nakatsuji, M. Caricato, X. Li, H.P. Hratchian, A.F. Izmaylov, J. Bloino, G. Zheng, J.L. Sonnenberg, M. Hada, M. Ehara, K. Toyota, R. Fukuda, J. Hasegawa, M. Ishida, T. Nakajima, Y. Honda, O. Kitao, H. Nakai, T. Vreven, J.A. Montgomery Jr., J.E. Peralta, F. Ogliaro, M. Bearpark, J.J. Heyd, E. Brothers, K.N. Kudin, V.N. Staroverov, R. Kobayashi, J. Normand, K. Raghavachari, A. Rendell, J.C. Burant, S.S. Iyengar, J. Tomasi, M. Cossi, N. Rega, N.J. Millam, M. Klene, J.E. Knox, J.B. Cross, V. Bakken, C. Adamo, J. Jaramillo, R. Gomperts, R.E. Stratmann, O. Yazyev, A.J. Austin, R. Cammi, C. Pomelli, J.W. Ochterski, R.L. Martin, K. Morokuma, V.G. Zakrzewski, G.A. Voth, P. Salvador, J.J. Dannenberg, S. Dapprich, A.D. Daniels, Ö. Farkas, J.B. Foresman, J.V. Ortiz, J. Cioslowski, D.J. Fox, Gaussian, Inc., Wallingford CT, 2009.

[10] GaussView, Guassian, Inc. (Carnergie Office Parck-Building6 Pittsburgh PA 151064 USA), Copyright © 2000-2003 Semichem. Inc.

[11] C. Lee, W. Yang, R.G. Parr, Phys. Rev. B 37 (785) (1988) 510.

[12] S.C. Zimmerman, P.S. Corbin, Heteroaromatic Modules for Self-Assembly Using Multiple Hydrogen Bonds. Molecular Self-Assembly Organic versus Inorganic Approaches, 2000, pp. 63–94.

[13] T. Lu, F. Chen, Multiwfn: a multifunctional Wavefunction analyzer, J. Comptu. Chem. 33 (2012) 580–592.

[14] C. Karaca, A. Atac, M. Karabacak, Conformational analysis, spectroscopic study (FT-IR, FT-Raman, UV, 1H and 13C NMR), molecular orbital energy and NLO properties of 5-iodosalicylic acid, Spectrochim. Acta Part A Mol. Biomol. Spectrosc. 136 (2015) 295–305.

[15] S.K. Wolff, D.J. Grimwood, J.J. McKinnon, M.J. Turner, D. Jayatilaka, M.A. Spackman, Crystal Explorer (Version 3.1), UWA, 2012.

[16] P. Pulay, G. Fogarasi, G. Pongor, J.E. Boggs, A. Vargha, Combination of theoretical ab initio and experimental information to obtain reliable harmonic force constants. Scaled quantum mechanical (QM) force fields for glyoxal, acrolein, butadiene, formaldehyde, and ethylene, J. Am. Chem. Soc. 105 (1983) 7073.

[17] a) G. Rauhut, P. Pulay, Transferable scaling factors for density functional derived vibrational force fields, J. Phys. Chem. 99 (1995) 3093–3099; b) G. Rauhut, P. Pulay, J. Phys. Chem. 99 (1995) 14572.

[18] T. Sundius, Scaling of ab-initio force fields by MOLVIB, Vib. Spectrosc. 29 (2002) 89–95.

[19] N.M. O'boyle, A.L. Tenderholt, K.M. Langner, Cclib: a library for package-independent computational chemistry algorithms, J. Comput. Chem. 29 (5) (2008) 839–845.

[20] http://www.rcsb.org/pdb/.

[21] J.M. Yang, C.C. Chen, GEMDOCK: a generic evolutionary method for molecular docking, Proteins Struct. Funct. Bioinform. 55 (2004) 288–304.

[22] D.S. Visualizer, Accelrys Software Inc. Discovery Studio Visualizer, 2005, p. 2.

[23] R.F.W. Bader, Atoms in Molecules, a Quantum Theory, Oxford University Press, 1990.

[24] R.F.W. Bader, M.A. Austen, Properties of atoms in molecules: atoms under pressure, J. Chem. Phys. 107 (11) (1997) 4271–4285.

[25] C. Reichardt, T. Welton, Solvent effects on the absorption spectra of organic compounds, Solv. Solv. Eff. Org. Chem. 4 (2011) 359–508.

[26] A.H. Pakiari, K. Eskandari, The chemical nature of very strong hydrogen bonds in some categories of compounds, J. Mol. Struct. (Theochem) 759 (2006) 51–59.

[27] E. Espinosa, E. Molins, C. Lecomte, Hydrogen bond strengths revealed by topological analyses of experimentally observed electron densities, Chem. Phys. Lett. 285 (3-4) (1998) 170–173.

[28] U. Koch, P. Popelier, Characterization of CHO hydrogen bonds on the basis of the charge density, Phys. Chem. 99 (1995) 9747–9754.

[29] A.D. Becke, K.E. Edgecombe, A simple measure of electron localization in atomic and molecular systems, J. Chem. Phys. 92 (1990) 5397–5403.

[30] B. Silvi, A. Savin, Classification of chemical bonds based on topological analysis of electron localization functions, Nature 371 (1994) 683.

[31] J.C. Prasana, S. Muthu, C.S. Abraham, Molecular docking studies, charge transfer excitation and wave function analyses (ESP, ELF, LOL) on valacyclovir: a potential antiviral drug, Comput. Biol. Chem. 78 (2019) 9–17.

[32] A. Sagaama, N. Issaoui, O. Al-Dossary, A.S. Kazachenko, M.J. Wojcik, SNon covalent interactions and molecular docking studies on morphine compound, J. King Saud Univ. Sci. 33 (2021) 101606.

[33] T. Ben Issa, A. Sagaama, N. Issaoui, Computational study of 3-thiophene acetic acid: molecular docking, electronic and intermolecular interactions investigations, Comput. Biol. Chem. 86 (2020) 107268.

[34] I. Jomaa, O. Noureddine, S. Gatfaoui, N. Issaoui, T. Roisnel, H. Marouani, Experimental, computational, and in silico analysis of (C8H14N2)2[CdCl6] compound, J. Mol. Struct. 12135 (2020) 128186.

[35] A. Sagaama, S.A. Brandan, T. Ben Issa, N. Issaoui, Searching potential antiviral candidates for the treatment of the 2019 novel coronavirus based on DFT calculations and molecular docking, Heliyon 6 (8) (2020), e04640.

[36] S. Gatfaoui, N. Issaoui, T. Roisnel, H. Marouani, Synthesis, experimental and computational study of a non-centrosymmetric material 3-methylbenzylammonium, J. Mol. Struct. 1225 (2020) 129132.

[37] M.A. Spackman, Molecular electric moments from x-ray diffraction data, Chem. Rev. 92 (1992) 197–1769.

[38] A. Volkov, P. Coppens, Calculation of electrostatic interaction energies in molecular dimers from atomic multipole moments obtained by different methods of electron density partitioning, J. Comput. Chem. 25 (7) (2004) 921–934.

[39] S.A.M. Safbri, Halim, M.M. Jotani, E.R. Tiekink, Bis [N-(2-hydroxyethyl)-N-isopropyldithiocarbamato-κ2S, S'](piperazine-κN) cadmium: crystal structure and Hirshfeld surface analysis, Acta Crystallogr. Sect. E: Crystallogr. Commun. 72 (2) (2016) 158–163.

[40] S. Syed, M.M. Jotani, S.N.A. Halim, E.R. Tiekink, A 2: 1 co-crystal of 2-methyl-benzoic acid and N, N'-bis (pyridin-4-ylmethyl) ethanediamide: crystal structure and Hirshfeld surface analysis, Acta Crystallogr. Sect. E: Crystallogr. Commun. 72 (3) (2016) 391–398.

[41] M.M. Jotani, S. Syed, S.N.A. Halim, E.R. Tiekink, 2-({[[Pyridin-1-ium-2-ylmethyl) carbamoyl] formamido} methyl) pyridin-1-ium bis (3, 5-dicarboxybenzoate): crystal structure and Hirshfeld surface analysis, Acta Crystallogr. Sect. E: Crystallogr. Commun. 72 (2) (2016) 241–248.

[42] C. Jelsch, K. Ejsmont, L. Huder, The enrichment ratio of atomic contacts in crystals, an indicator derived from the Hirshfeld surface analysis, IUCrJ 1 (2) (2014) 119–128.

[43] E.R. Johnson, S. Keinan, P. Mori-S_anchez, J. Contreras-García, A.J. Cohen, W. Yang, Revealing noncovalent interactions, J. Am. Chem. Soc. 132 (18) (2010) 6498–6506.

[44] E.R. Johnson, S. Keinan, P. Mori-Sanchez, J. Contreras-García, A.J. Cohen, W. Yang, Revealing noncovalent interactions, Am. Chem. Soc. 132 (2010) 6498–6506.

[45] M.T. Alotaibi, Noncovalent interaction stabilizes the 2, 4-Dinitrophenylhydrazone Derivatives over g-C3N4 surface to enhance optical properties: synthesis, characterization, and DFT investigation, J. Mol. Struct. (2020) 128192.

[46] N.Q. Su, X. Xu, Insights into direct methods for predictions of ionization potential and electron affinity in density functional theory, J. Phys. Chem. Lett. 10 (11) (2019) 2692–2699.

[47] T. Vreven, K.S. Byun, I. Kómáromi, S. Dapprich Jr., J.A. Montgomery, K. Morokuma, M.J. Frisch, Combining quantum mechanics methods with molecular mechanics methods in ONIOM, J. Chem. Theor. Comput. 2 (3) (2006) 815–826.

[48] A. Sagaama, N. Issaoui, Design, molecular docking analysis of an anti-inflammatory drug, computational analysis and intermolecular interactions energy studies of 1-benzothiophene-2-carboxylic acid, Comput. Biol. Chem. 88 (2020) 107348.

[49] F.J. Luque, J.M. López, M. Orozco, Perspective on "Electrostatic interactions of a solute with a continuum. A direct utilization of ab initio molecular potentials for the prevision of solvent effects", Theor. Chem. Acc. 103 (3) (2000) 343–345.

[50] A. Sagaama, O. Noureddine, S.A. Brandán, A. Jarczyk-Jędryka, H.T. Flakus, H. Ghalla, N. Issaoui, Molecular docking studies, structural and spectroscopic properties of monomeric and dimeric species of benzofuran-carboxylic acids derivatives: DFT calculations and biological activities, Comput. Biol. Chem. 87 (2020) 107311.

[51] I. Fleming, Frontier Orbitals and Organic Chemical Reactions, Wiley, London, 1976.

[52] G. Gece, The use of quantum chemical methods in corrosion inhibitor studies, Corrosion Sci. 50 (11) (2008) 2981–2992.

[53] L. Padmaja, C. Ravikumar, D. Sajan, I. Hubert Joe, V.S. Jayakumar, G.R. Pettit, O. Faurskov Nielsen, Density functional study on the structural conformations and intramolecular charge transfer from the vibrational spectra of the anticancer drug combretastatin A2, J. Raman Spectrosc.: Int. J. Orig. Work Asp. Raman Spectr. Includ. Higher Order Proc. Brillouin Rayleigh Scatt. 40 (4) (2009) 419–428.

[54] T.H. Wang, I.T. Wang, W.L. Huang, L.Y. Huang, A DFT study on structures, frontier molecular orbitals and UV–vis spectra of RuX (PPh3)(NHCPh2) L (X= Tp and Cp; L= Cl and N3), Spectrochim. Acta A Mol. Biomol. Spectrosc. 121 (2014) 650–656.

[55] S. Gatfaoui, A. Mezni, T. Roisnel, H. Marouani, Synthesis, characterization, Hirshfeld surface analysis and antioxidant activity of a novel organic-inorganic hybrid material 1-methylpiperazine-1, 4-diium bis (nitrate), J. Mol. Struct. 1139 (2017) 52–59.

[56] S. Gatfaoui, N. Issaoui, A. Mezni, F. Bardak, T. Roisnel, A. Atac, H. Marouani, Synthesis, structural and spectroscopic features, and investigation of bioactive nature of a novel organic-inorganic hybrid material 1H-1,2,4-triazole-4-ium trioxonitrate, J. Mol. Struct. 1150 (2017) 242–257.

[57] S. Gatfaoui, N. Issaoui, T. Roisnel, H. Marouani, Synthesis, experimental and computational study of a non-centrosymmetric material 3-methylbenzylammonium, J. Mol. Struct. 1225 (2020) 129132.

[58] N. Issaoui, H. Ghalla, S. Muthu, H.T. Flakus, B. Oujia, Molecular structure, vibrational spectra, AIM, HOMO–LUMO, NBO, UV, first order hyperpolarizability, analysis of 3-thiophenecarboxylic acid monomer and dimer by Hartree–Fock and density functional theory, Spectrochim. Acta Part A Mol. Biomol. Spectrosc. 136 (2015) 1227–1242.

[59] M. Medimagh, N. Issaoui, S. Gatfaoui, O. Al-Dossary, A. S. Kazachenko, H. Marouani, M.J. Wojcik, Molecular modeling and biological activity analysis of new organic-inorganic hybrid: 2-(3,4-dihydroxyphenyl) ethanaminium nitrate, J. King Saud Univ. Sci. 33 (2021) 101616.

[60] M.M. El-Nahass, M.A. Kamel, A.F. El-Deeb, A.A. Atta, S.Y. Huthaily, Density functional theory (DFT) investigation of molecular structure and frontier molecular orbitals (FMOs) of PN, N-dimethylaminobenzylidenemalononitrile (DBM), Spectrochim. Acta A Mol. Biomol. Spectrosc. 79 (5) (2011) 1499–1504.

[61] G. Keresztury, S. Holly, G. Besenyei, J. Varga, A.Y. Wang, J.R. Durig, Vibrational spectra of monothiocarbamates-II. IR and Raman spectra, vibrational assignment, conformational analysis and ab initio calculations of S-methyl-N,N-dimethylthiocarbamate, Spectrochim. Acta 49A (1993) 2007–2026.

[62] D. Michalska, R. Wysokinski, The prediction of Raman spectra of platinum(II) anticancer drugs by density functional theory, Chem. Phys. Lett. 403 (2005) 211–217.

[63] N. Issaoui, N. Rekik, B. Oujia, M.J. Wójcik, Anharmonic effects on theoretical IR line shapes of medium strong H(D) bonds, Int. J. Quant. Chem. 109 (3) (2009) 483–499.

[64] N. Issaoui, N. Rekik, B. Oujia, M.J. Wójcik, Theoretical infrared line shapes of H-bonds within the strong anharmonic coupling theory and fermi resonances effects, Int. J. Quant. Chem. 110 (14) (2010) 2583–2602.

[65] N. Rekik, N. Issaoui, H. Ghalla, B. Oujia, M.J. Wójcik, IR spectral density of H-bonds. Both intrinsic anharmonicity of the fast mode and the H-bond Bridge. Part I: anharmonic coupling parameter and temperature effects, J. Mol. Struct.: Theochem 821 (2007) 1–3, 9 – 211.

[66] S.A. Brandán (Ed.), Nitrate: Occurrence, Characteristics and Health Considerations, Nova Science Publishers, Inc, 2012. Edited Collection.

[67] S.A. Brandán, in: Ken Derham (Ed.), A Structural and Vibrational Study of the Chromyl Chlorosulfate, Fluorosulfate, and Nitrate Compounds, vol. 1, Springer Science, Business Media B.V., Van Godewijckstraat, 30, 2012, p. 3311. GZ Dordrecht, Netherlands.

[68] M.V. Castillo, E. Romano, H.E. Lanús, S.B. Díaz, A. Ben Altabef, S.A. Brandán, Theoretical structural and experimental vibrational study of niobyl nitrate, J. Mol. Struct. 994 (2011) 202–208.

[69] D. Romani, S.A. Brandán, Structural and spectroscopic studies of two 1,3-benzo-thiazole tautomers with potential antimicrobial activity in different media. Prediction of their reactivities, Comput. Theor. Chem. (Theochem) 1061 (2015) 89–99.